NAVAL POSTGRADUATE SCHOOL

MONTEREY, CALIFORNIA

THESIS

IMPROVING ACCURACY OF ACOUSTIC PREDICTION IN THE PHILIPPINE SEA THROUGH INCORPORATION OF MESOSCALE ENVIRONMENTAL EFFECTS

by

Kimberly M. Freitas

June 2008

Thesis Advisor: John A. Colosi
Second Reader: Jeffrey D. Paduan

Approved for public release; distribution is unlimited.

THIS PAGE INTENTIONALLY LEFT BLANK

REPORT DOCUMENTATION PAGE		*Form Approved OMB No. 0704-0188*

1. AGENCY USE ONLY *(Leave blank)*	2. REPORT DATE June 2008	3. REPORT TYPE AND DATES COVERED Master's Thesis

4. TITLE AND SUBTITLE Improving Accuracy of Acoustic Prediction in the Philippine Sea through Incorporation of Mesoscale Environmental Effects	5. FUNDING NUMBERS
6. AUTHOR(S) Kimberly Freitas	
7. PERFORMING ORGANIZATION NAME(S) AND ADDRESS(ES) Naval Postgraduate School Monterey, CA 93943-5000	**8. PERFORMING ORGANIZATION REPORT NUMBER**
9. SPONSORING /MONITORING AGENCY NAME(S) AND ADDRESS(ES) N/A	**10. SPONSORING/MONITORING AGENCY REPORT NUMBER**

11. SUPPLEMENTARY NOTES The views expressed in this thesis are those of the author and do not reflect the official policy or position of the Department of Defense or the U.S. Government.

12a. DISTRIBUTION / AVAILABILITY STATEMENT Approved for public release; distribution is unlimited.	12b. DISTRIBUTION CODE

13. ABSTRACT (maximum 200 words)

An understanding of ocean acoustic fields, their statistics, and relation to the oceanographic environment is the sine qua non of undersea warfare. In the tactically important Philippine Sea, powerful mesoscale eddies can have strong effects on acoustic fields. To quantify eddy effects, a mesoscale sound-speed model was developed and interfaced with a parabolic equation acoustic simulation. Eight combinations of frequency (20Hz/250Hz), wavenumber spectra (Stammer/Lorentzian), and source depth (50m/200m) were simulated through the model. For each combination, the unperturbed transmission loss (TL) curve and composite eddy-field TL curve were compared to assess acoustic variability caused by mesoscale ocean features. Eddies alter acoustic energy by shifting convergence zones, driving energy into the seabed, trapping energy in surface ducts, and increasing scintillation. These effects are greater at higher frequencies and deeper source depths, shifting both the mean TL difference and RMS variability on order 5-10dB. The wavenumber spectrum showed no significant effect on acoustic variability. Eddies also cause horizontal out-of-plane scattering. Ray equations were manipulated to demonstrate that eddy-induced bearing-angle errors can be on order one degree at 500km, increasing as the square-root of range. Target localization errors due to angle error are on order 7km at 500km, increasing as range to 3/2 power.

14. SUBJECT TERMS Ocean acoustic prediction, mesoscale eddies, parabolic equations, Monte Carlo simulation, Philippine Sea, three-dimensional acoustics, undersea warfare, tomography, battlespace characterization	15. NUMBER OF PAGES 69
	16. PRICE CODE

17. SECURITY CLASSIFICATION OF REPORT Unclassified	18. SECURITY CLASSIFICATION OF THIS PAGE Unclassified	19. SECURITY CLASSIFICATION OF ABSTRACT Unclassified	20. LIMITATION OF ABSTRACT UU

THIS PAGE INTENTIONALLY LEFT BLANK

**IMPROVING ACCURACY OF ACOUSTIC PREDICTION
IN THE PHILIPPINE SEA THROUGH INCORPORATION OF
MESOSCALE ENVIRONMENTAL EFFECTS**

Kimberly M. Freitas
Lieutenant, United States Navy
B.S., Pennsylvania State University, 2000

Submitted in partial fulfillment of the
requirements for the degree of

**MASTER OF SCIENCE IN
METEOROLOGY AND PHYSICAL OCEANOGRAPHY**

from the

**NAVAL POSTGRADUATE SCHOOL
June 2008**

Author: Kimberly M. Freitas

Approved by: John A. Colosi
                 Thesis Advisor

                 Jeffrey D. Paduan
                 Second Reader

                 Mary L. Batteen
                 Chairman, Department of Oceanography

THIS PAGE INTENTIONALLY LEFT BLANK

ABSTRACT

An understanding of ocean acoustic fields, their statistics, and relation to the oceanographic environment is the *sine qua non* of undersea warfare. In the tactically important Philippine Sea, powerful mesoscale eddies can have strong effects on acoustic fields. To quantify eddy effects, a mesoscale sound-speed model was developed and interfaced with a parabolic equation acoustic simulation. Eight combinations of frequency (20Hz/250Hz), wavenumber spectra (Stammer/Lorentzian), and source depth (50m/200m) were simulated through the model. For each combination, the unperturbed transmission loss (TL) curve and composite eddy-field TL curve were compared to assess acoustic variability caused by mesoscale ocean features. Eddies alter acoustic energy by shifting convergence zones, driving energy into the seabed, trapping energy in surface ducts, and increasing scintillation. These effects are greater at higher frequencies and deeper source depths, shifting both the mean TL difference and RMS variability on order 5-10dB. The wavenumber spectrum showed no significant effect on acoustic variability. Eddies also cause horizontal out-of-plane scattering. Ray equations were manipulated to demonstrate that eddy-induced bearing-angle errors can be on order one degree at 500km, increasing as the square-root of range. Target localization errors due to angle error are on order 7km at 500km, increasing as range to 3/2 power.

THIS PAGE INTENTIONALLY LEFT BLANK

TABLE OF CONTENTS

THIS PAGE INTENTIONALLY LEFT BLANK

LIST OF FIGURES

LIST OF TABLES

THIS PAGE INTENTIONALLY LEFT BLANK

ACKNOWLEDGMENTS

I would like to express my heartfelt gratitude to Professor John Colosi for his inspiration, patience, and wealth of knowledge. Without his guidance and understanding over the past few months, this thesis would be more than incomplete. I'd also like to thank Professor Jeff Paduan for the mesoscale knowledge he contributed to the project. Many thanks go out to Chris Miller (and Pippin) without whom the computer processing portion of the thesis would have been unbearable, and to Mike Cook for initially instilling MATLAB knowledge in my head. Several professors at NPS have been inspiring researchers and instructors: Timour Radko, Les Carr, Pat Harr, J.J. Joseph, and Ching-Sang Chiu. Thank you for your hard work. For Captain Katz, thank you for always being a wise sounding board and for teaching us all to have fun AND be the professional military officers that we're supposed to be.

To the NPAL group – thank you for letting me join in your workshop. It was inspiring and overwhelming at the same time. I wish you all the best with the upcoming experiments.

To the students and friends who came before me, those with whom I worked, and those who will follow – this NPS experience would be worth nothing without your friendships. Despite being happy to graduate, I will miss you all.

My family has been an amazing support during this whole process, so I'd like to acknowledge their contributions as well. To Mom and Dad, thanks for always being there, for always supporting me no matter how large a bite I thought I could handle, and for keeping me calm when I realized just how big that bite was. To my wonderful husband, Pedro – I'm glad you went through this first! And I'm so thankful to have you in my life, even if you're not always physically nearby. This past year has been an amazing journey, and I'm so happy you've been by my side (at least virtually) through it all. Thank you for your support, encouragement, and devotion.

THIS PAGE INTENTIONALLY LEFT BLANK

I.   INTRODUCTION

The kinetic energy associated with ocean circulation is 99% contained within mesoscale ocean features having horizontal spatial scales less than 100km [Munk et al. 1995]. Ocean mesoscale processes include fronts, jets, filaments, squirts, eddies, and meanders [Stammer 1997]. Variability in kinetic energy can lead to significant differences in sound speed through seawater. Ocean eddies, one specific family of mesoscale features, produce sound speed fluctuations of order 5-15 m/s root mean square (RMS) that are superimposed on the background sound speed profile [Munk et al. 1995]. Typical scales of these eddies are hundreds of meters in the vertical, hundreds of kilometers in the horizontal, and weeks to months in duration [Stammer 1997, Kobashi and Kawamura 2001]. As such, these features can lead to important variations in acoustic fields to be used in signal detection, classification, and localization.

A.   PREVIOUS WORK AND LINKS TO FUTURE PROJECTS

Over sixty years of ocean acoustic research exists, prompted by the discovery of the deep sound channel in 1944 [Worcester and Spindel 2005]. Observationally, eddy effects on acoustic variability were documented as early as 1973 [Vastano and Owens 1973], but present theory and computer modeling are quite limited [Smith et al. 1992, Munk et al. 1995].

More recently, the North Pacific Acoustic Laboratory (NPAL) commenced research and experimentation in the field of acoustic variability as influenced by the mesoscale environment. These and other experiments have led to some quantification of eddy effects on propagation loss and horizontal diffraction [Kirby 1988, Weinberg and Clark 1980], but a theoretical basis for understanding these effects is still insufficient [Worcester and Spindel 2005]. Further work in prediction of eddy effects has been accomplished by Cornuelle and Howe [1987]; Smith et al. [1992]; and Munk et al. [1995].

Cornuelle and Howe [1987] studied eddy-induced ray loop resonances and demonstrated that eddies with wavelengths near the ray loop length have the greatest

effect on acoustics. Smith et al.[1992] examined ray chaos as it applies to eddy effects. This research suggests that deterministic predictions for near-axial acoustic energy using ray theory are valid at ranges less than one to two thousand kilometers. Munk et al. [1995] discussed ray loop resonance, as well as horizontal angle deviation through a single theoretical eddy.

Up to this point, previous work has not had much emphasis on transmission loss curves or three-dimensional acoustic processes, such as horizontal out-of-plane refraction caused by ocean eddies. This study is designed as a small part of the larger upcoming field exercise by NPAL in the Philippine Sea. Thorough understanding of the expected ocean variability due to the mesoscale environment will allow better development of the experimental plan. Additionally, quantification of the eddy-induced acoustic intensity change measures the value of accurately mapping the mesoscale ocean environment.

The most current version of the NPAL Philippine Sea Experiment plan as of April 2008 is designed around a six-node transceiver array for acoustic tomography, as shown in Figure 1. The experiment aims to characterize the barotropic and baroclinic structure of the ocean environment, spatially and temporally, in order to generate an eddy-resolving, four-dimensional sound speed field for acoustic predictions. The scientific goals, from the Strawman Philippine Sea Experiment Plans [working document from NPAL 11th Annual Workshop, April 2008], are to:

> (i) understand the impacts of fronts and eddies on acoustic propagation in this highly variable region, (ii) determine whether acoustic methods, together with satellite, glider and other measurements and coupled with ocean modeling, can yield estimates of the time-evolving ocean state useful for making improved acoustic predictions and for understanding the local ocean dynamics, (iii) improve our understanding of the basic physics of scattering by small-scale oceanographic variability due to internal waves and spice, and (iv) characterize the ambient noise field, particularly its variation over the year and its depth dependence.
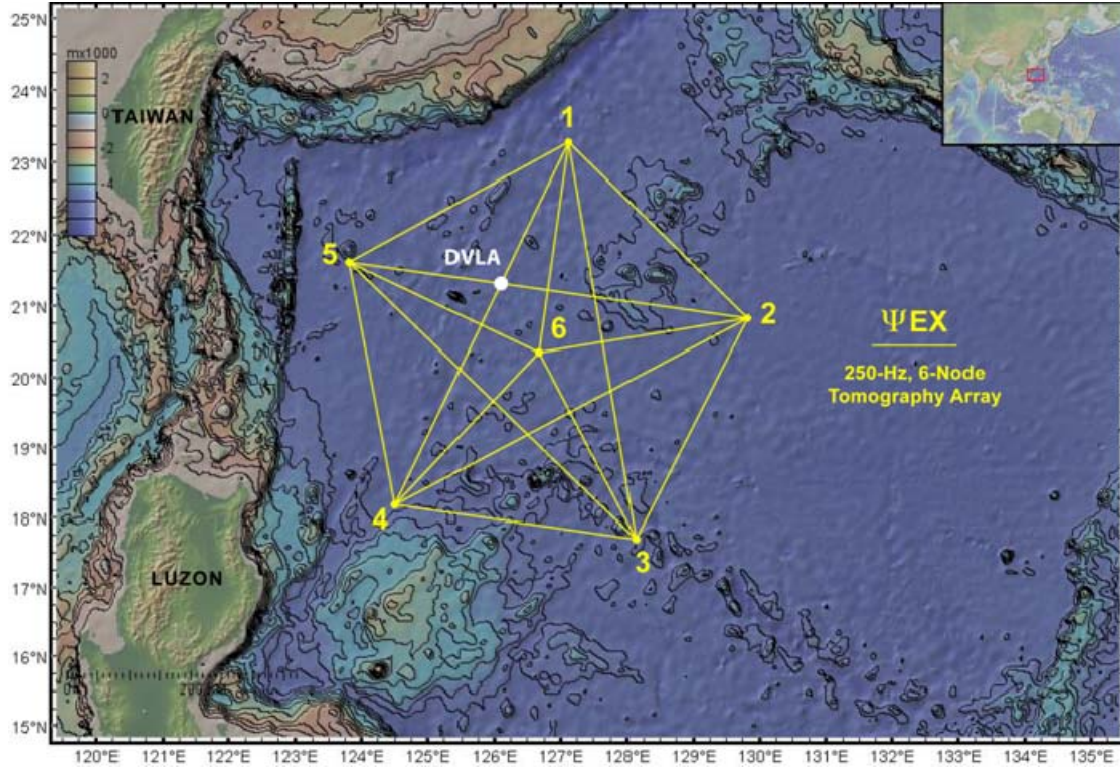
Figure 1.   Array node locations, as currently proposed, for upcoming NPAL field experiment in the Philippine Sea in 2009-2011. Color bar denotes underwater bathymetry. Contours from 500m to 5000m are shown, at 500m intervals. [Strawman Philippine Sea Experiment Plans, working document from NPAL 11th Annual Workshop, April 2008]

B.   MOTIVATION AND STATEMENT OF RESEARCH

Thoroughly understanding the ocean acoustic fields, their statistics, and their relation to the oceanographic environment is the *sine qua non* of undersea warfare. Eddies are dynamic features which can cause large sound speed fluctuations because they have different physical properties than the ocean around them. These localized acoustic fluctuations on order 10dB can have significant effects on target detection and targeting accuracy. Observationally, physical processes by which eddies affect transmission loss are: causing increased scintillation, shifting convergence zone ranges, driving energy into the seabed, and forcing energy into a surface duct.

Eddies are unlike internal waves in that they can be modeled deterministically. Theoretically, these deterministic models will allow scientists to predict the magnitude of eddy-induced sound speed variability.

Additionally, eddies refract sound out of the horizontal plane, which affects beam forming capabilities and accuracy of bearing angle measurements. Previous research has shown horizontal refraction through mesoscale eddies and fronts ranging from 0.5 to several degrees [Munk 1980, Weinberg and Clark 1980].

In order to further investigate the points listed above, the objectives of this study are to:

- identify the important eddy scales,

- assess the feasibility of constructing a useful mesoscale model based upon present observations that can be used for acoustic prediction calculations,

- quantify the effects of eddies on transmission loss estimates based on numerical simulation,

- analyze the importance of out-of-plane scattering effects.

Chapter II describes basic principles used in creating the acoustic model. Chapter III discusses methods of analysis, including the parabolic equation method, the boundary conditions for the computational domain, and modeling of the ocean background and eddy fields. Chapter IV addresses the results of the computer simulations, and Chapter V provides some conclusions and statements regarding future work.

II. BASIC PRINCIPLES

A. ROSSBY WAVES

In this study, eddies are modeled as superpositions of linear Rossby waves, as in the treatment by Munk et al. [1995]. This method is convenient in that it allows computationally efficient modeling of non-linear eddies using linear methods that produce similar temporal and spatial scales. As shown in Figure 2, Rossby wave dynamics are unique in that the dispersion relation is circular:

$$\sigma = -\beta k_x / (k_x^2 + k_y^2 + \lambda^2). \tag{1}$$

Here, σ is the Rossby wave frequency, β is the latitudinal gradient of Coriolis force, and k_x and k_y are horizontal wavenumbers. The Rossby eigenvalue is represented by λ, where $1/\lambda$ is the Rossby radius of deformation (the length scale at which rotational effects and buoyancy effects are equally important).

High frequency Rossby waves have small wavenumbers and long wavelengths, while low frequency Rossby waves have large wavenumbers and short wavelengths. Low frequency (less than one cycle per year), large wavenumber Rossby waves are used here to represent mesoscale eddies that have the most effect on acoustics, because they are scaled near the ray loop length [Cornuelle and Howe 1987].
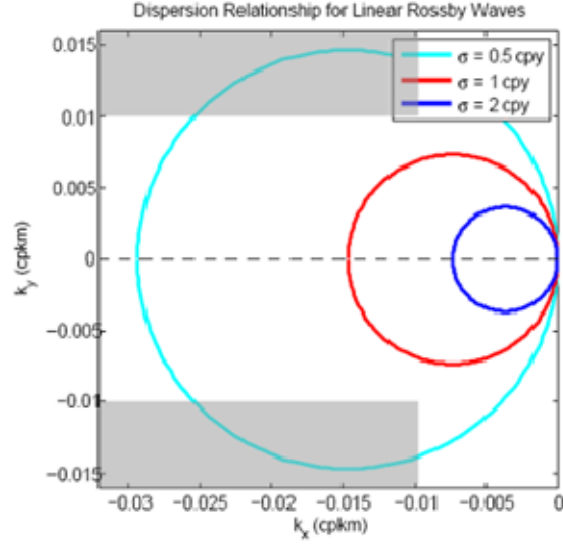
Figure 2.   Rossby wave dispersion relations for σ =0.5, 1, and 2 cycles per year. The shaded regions represent those Rossby waves that most affect acoustic propagation.

B.   GLOBAL WAVENUMBER SPECTRA

Until Stammer's work in 1997, eddy dynamics had not been well understood, due in part to the inadequacy of available ocean observing systems. However, the forcing mechanisms for eddies and the methods by which eddies disperse energy are particularly important to understand because 99% of the ocean kinetic and potential energy is carried and redistributed through eddies [Stammer 1997].

Satellite altimetry provides a global observation system, and therefore, can be a valuable tool in gaining insight into mesoscale ocean features. Stammer [1997] analyzed three years of sea surface height (SSH) data from the TOPEX/Poseidon (T/P) satellite altimeter and derived a universal spectral model of SSH to infer scales of ocean variability in specific ocean regions.

6

The linear relationship between the first-mode Rossby radius of deformation and the eddy scale suggests that first-mode processes dominate SSH variations. Stammer derived a global spectral relation for SSH, displayed in Figures 3 and 4a:

$$
S_\zeta(\tilde{k}) = \begin{cases} 135\tilde{k}^{-0.7} & 0.18 \le \tilde{k} \le 1.006 \\ 135\tilde{k}^{-2.8} & 1.006 \le \tilde{k} \le 2.057 \\ 135\tilde{k}^{-4.6} & 2.057 \le \tilde{k} \le 4.54, \end{cases} \tag{2}
$$

by normalizing the along-track wavenumber by the local eddy wavenumber of maximum energy ($\tilde{k} = k/k_0$).
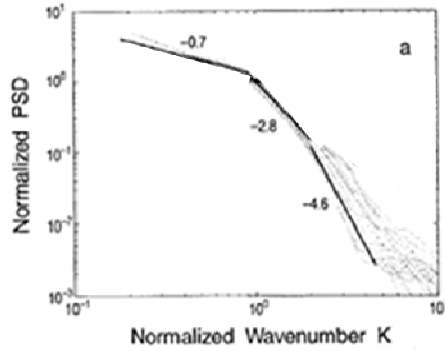
Figure 3.   Zonal averaged wavenumber spectrum normalized by k_0, the local wavenumber of maximum energy. (After Stammer 1997.)

Stammer's results indicate baroclinic instability is the dominant eddy source in the extratropical oceans. Within the framework of baroclinic instability, the Rossby radius of deformation is closely related to the spatial scale of maximum eddy growth rates. In observation, non-linear processes act to increase the length scales of the most unstable waves.

In addition to the spectrum designed by Stammer, another power spectrum, colloquially named the Lorentzian spectrum and shown in Figure 4b, is another method to describe the wavenumber relation for the mesoscale ocean:

$$
S_\zeta(k_h) = \frac{2}{\pi} \frac{k_*}{k_h^2 + k_*^2}, \tag{3}
$$

where $k_* = 1/300\,\text{km}$ and $k_h = k_x, k_y$ are horizontal wavenumbers [Munk et al. 1995].

7
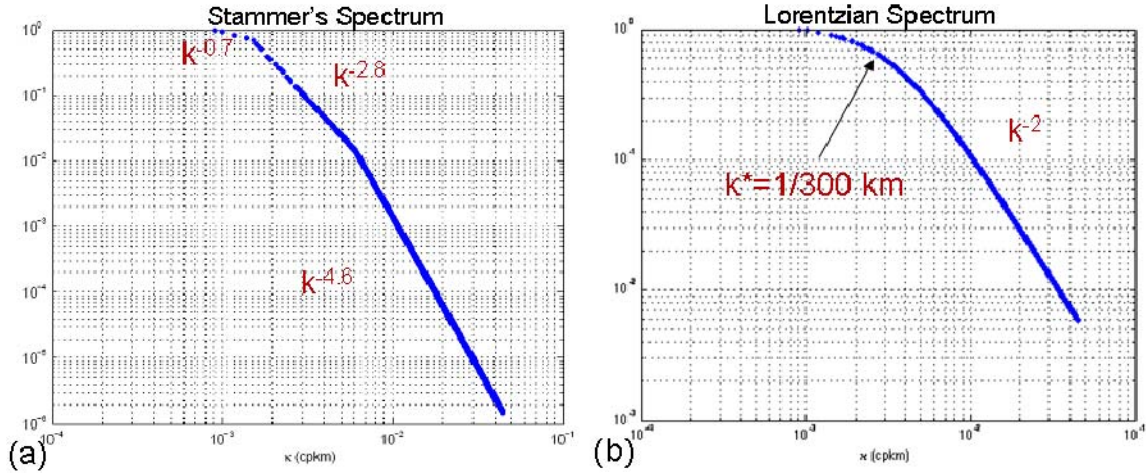
Figure 4.   (a) Modeled wavenumber eddy spectrum as designed by Stammer [1997], where frequency is a power function of wavenumber. Power values for each slope are indicated.   (b) Modeled Lorentzian wavenumber eddy spectrum [Munk et al. 1995], where frequency is a power function of wavenumber at the higher values of wavenumber, but rolls off at k* as indicated.

C.   VERTICAL PARTITIONING OF KINETIC ENERGY IN THE OCEAN

Sea surface altimetry provides valuable information in quantifying ocean energy at the surface; however, understanding the vertical structure of the ocean is essential to properly assessing the altimetry-derived sea surface elevation and slope. Wunsch studied two decades of moored current meter observations from many sources and devised a reasonable first estimate of vertical partitioning of the ocean. Further work is still necessary due to the disparate spatial and temporal nature of the data; however these results are a good starting point [Wunsch 1997].

For the main portion of the North Pacific Ocean (bounded by 135º and 245ºE and 25º and 60ºN), about 35% of total kinetic energy is contained in the barotropic mode, with the remaining 65% in baroclinic modes. In the area of the NPAL experiment, approximately 30% kinetic energy is contained in the barotropic mode, 40% in the first baroclinic mode, 10% in the second baroclinic mode, and the remainder in higher modes. In terms of surface kinetic energy, as much as 90% of the energy is contributed from the baroclinic modes in parts of the North Pacific.

These findings are based on scarce data, few degrees of freedom, and considerable subjectivity in contouring; however, they are validated by altimeter measurements. The extrapolations of current meter modes to surface kinetic energy match up fairly well compared to the altimetric surface kinetic energy distribution. A useful outcome of the NPAL experiment will be a quantitative measure of proportional mode energy in Philippine Sea eddies.

THIS PAGE INTENTIONALLY LEFT BLANK

III. METHODS OF ANALYSIS

A. PARABOLIC EQUATION METHOD

1. The Parabolic Equation

Introduced to underwater acoustics in 1973 by R. H. Hardin and F. D. Tappert, the parabolic equation (PE) method is an efficient means of solving wave propagation problems [Jensen et al. 2000]. The PE techniques have been continually advanced within the acoustic modeling community, and they are now the most common method of resolving range-dependent underwater acoustic propagation [Jensen et al. 2000]. The following PE derivation is closely aligned with that in Jensen et al [2000].

Beginning with the Helmholtz equation, which describes acoustic pressure as a function of range (r), azimuth (φ), and depth (z), azimuthal symmetry is assumed so that the φ-coordinate can be ignored. This yields a description of acoustic pressure as a function of range and depth, $p(r,z)$, and the Helmholtz equation becomes:

$$\frac{\partial^2 p}{\partial r^2} + \frac{1}{r}\frac{\partial p}{\partial r} + \frac{\partial^2 p}{\partial z^2} + k_0^2 n^2 p = 0 , \tag{4}$$

where $k_0 = \dfrac{\omega}{c}$ is the reference wavenumber, $n(r,z) = \dfrac{c_0}{c(r,z)}$ is the index of refraction, and $c(r,z) = \overline{c}(z) + \delta c(r,z)$. The solution of the Helmholtz equation is assumed to have the form

$$p(r,z) = \Psi(r,z) H_0^{(1)}(k_0 r) , \tag{5}$$

where $\Psi(r,z)$ is the wave envelope function and $H_0^{(1)}$ is a Hankel function of the first order.

By substituting equation (5) into (4) and making the small angle approximation,

$$\frac{\partial^2 \Psi}{\partial r^2} \ll 2ik_0 \frac{\partial \Psi}{\partial r},$$

(6)

the Helmholtz equation yields the standard parabolic equation as first introduced to underwater acoustics by Hardin and Tappert:

$$2ik_0 \frac{\partial \Psi}{\partial r} + \frac{\partial^2 \Psi}{\partial z^2} + k_0{}^2(n^2 - 1)\Psi = 0.$$

(7)

2. Solutions to the Parabolic Equation Using the Split Step Fourier Algorithm

Split step methods analytically solve partial differential equations in range-marching algorithms with two distinct steps. In this case, a solution is first calculated in the depth domain using a phase screen that includes refractive effects, and then the solution is advanced in the wavenumber domain for a homogenous medium including diffraction. This study uses the following Split Step Fourier algorithm described in Jensen et al.:

$$\Psi(r,z) = \mathcal{F}^{-1}\left\{ e^{-\frac{i\Delta r}{2k_0}} \mathcal{F}\left\{ e^{\frac{ik_0}{2}[n^2(r_0, z) - 1]\Delta r} \Psi(r_0, z) \right\} \right\},$$

(8)

where $\mathcal{F}$ is the fast Fourier transform (FFT) from the z-domain to the k_z-domain and $\mathcal{F}^{-1}$ is the inverse transform.

3. Set-up of the Computational Domain

Three distinct boundaries exist within the computational domain: the ocean surface or air-ocean interface, the ocean bottom or ocean-seafloor interface, and a "sponge" layer that is used beneath the seafloor to prevent computational wrap-around of energy by the Fourier transform solution.

Ocean acoustic analyses typically treat the surface as a pressure-release boundary, which is represented by the boundary condition $\Psi(r,0) = 0$. Within the PE model, this boundary condition is achieved by creating an image source. Similar to Lloyd's mirror, this setup causes any original-source sound at the surface to be canceled out by the image

source.   By subtracting the image source contribution from the original source contribution, the surface boundary condition is met:

$$\Psi(r,0) = \Psi(r,-z_s) - \Psi(r,z_s) = 0 ,$$ (9)

where z_s is the original source depth.

At the ocean-seafloor interface, the bottom sediment layer is important to propagation because of attenuation and the density change at the interface. Here, a variable-density layer is included in the numerical model to modify an effective index of refraction, where n_{eff} is density dependent. In a real ocean, the density difference at the ocean bottom is discontinuous, but this causes computational problems in solving the numerical algorithm. Hence, we use

$$\rho(z) = \frac{1}{2}(\rho_2 + \rho_1) + \frac{1}{2}(\rho_2 - \rho_1)\tanh\left(\frac{z - D_0}{L}\right),$$ (10)

where D_0 is the depth of the interface and L is the distance over which the density changes from ρ_1 to ρ_2, to represent the density discontinuity at the interface. L is defined such that $k_0 L = 2$.

Density of the water, ρ_1, is determined by the background ocean profile (discussed below), and density of the seafloor, $\rho_2 = 1800 \text{kg m}^{-3}$, is representative of a sandy, silty bottom.

Attenuation in the ocean bottom is treated by adding an imaginary part, $i\alpha$, to the wavenumber,

$$k = \frac{\omega}{c} + i\alpha, \ \alpha > 0$$ (11)

where α is defined as 1.11 dB/λ. This yields a complex index of refraction:

$$n(x,z)^2 = \left(\frac{k}{k_0}\right) \simeq \left(\frac{c_0}{c(x,z)}\right)^2 \left[1 + i\frac{2\alpha c_0}{\omega}\right],$$ (12)

which allows attenuation to be evaluated in range and depth.

Below the ocean-seafloor interface, the computational domain is treated with an artificially attenuating "sponge" layer, in order to absorb the periodic solution generated

13

by the FFT method. In the periodic FFT solution, energy at the bottom of the solution domain reenters the solution space at the top of the next cycle. Artificial attenuation in the sponge layer of the form,

$$L(z) = \exp\left\{-\beta dx \times \exp[-\left(\frac{z - z_b}{\alpha z_b}\right)^2]\right\}, \tag{13}$$

where z_b is the depth at the bottom of the computational field, negates this wrap-around effect by imposing a gradual loss of amplitude as z approaches the computational bottom [Colosi and Flatté 1996]. Here, β is the relative strength of the loss, and α is the location relative to the bottom at which loss is applied. As determined for this study, values of $\beta = 0.04$ and $\alpha = 0.05$ stop acoustic energy from penetrating beyond about 300m above the computational boundary, which is approximately 1000m deeper than the ocean-seafloor interface.

4.   Sound Source

A Gaussian sound source is used to closely align with the far-field, point-source solution of the Helmholtz equation. This source is defined as:

$$\Psi(0, z) = \sqrt{k_0}e^{-\frac{k_0^2}{2}(z - z_s)^2} \cdot 10^{SL/20}, \tag{14}$$

where $\sqrt{k_0}$ is the effective source level, $\frac{\sqrt{2}}{k_0}$ is the beamwidth, and SL is the source level (195dB). At the surface boundary, equation (9) is applied to the Gaussian sound source to yield the starting field:

$$\Psi(0, z) = \sqrt{k_0}\left[e^{-\frac{k_0}{2}(z - z_s)^2} - e^{-\frac{k_0}{2}(z + z_s)^2}\right] \cdot 10^{SL/20}. \tag{15}$$

The unperturbed wavenumber k_0 can be represented as $k_0 = \frac{2\pi f_0}{c_0}$ in terms of initial frequency, f_0, and initial sound speed, c_0. As an example, a close-up view of a full water-column transmission loss diagram is shown in Figure 5.

14
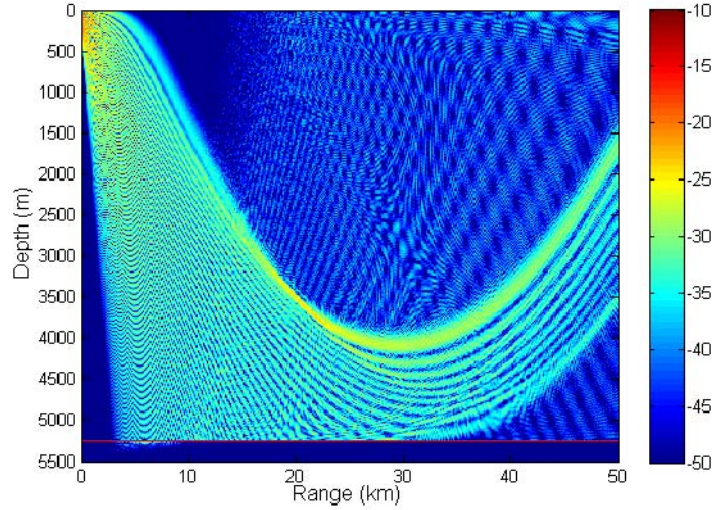
Figure 5.   Close-up view of transmission loss plot from 250Hz Gaussian point source in an unperturbed ocean at 200m depth.

The 250Hz point source in Figure 5 is at 200m and transmits sound energy in a conical range 45 degrees above and below horizontal. This 45 degree cone is visible below the horizontal, with the region void of acoustic energy represented by the dark blue sliver on the left hand side. In this case, the sound source is too close to the surface for the corresponding feature to be visible above the source. The modeled transmission loss plot shows the interference pattern of upward and downward acoustic rays, as well as interactions between the bottom reflections and transmitted energy at ranges greater than 10km. Within the first 10km, the acoustic rays are steep enough that they penetrate into the seafloor, but beyond 10km, energy is reflected off the bottom, causing the energy visible above the main ray loop.

B.   EDDY AND OCEAN MODELING

1.   Background Ocean

Background ocean profiles for the Philippine Sea were derived from the World Ocean Atlas 2001 database. Annual average profiles for temperature and salinity from the database were used to calculate sound speed, potential density, buoyancy frequency, and potential sound speed gradient profiles. Figure 6 shows the background ocean

15

profiles derived from the World Ocean Atlas at 23°N 125°E, which is northwest of the NPAL tomography array (Figure 1) in deep water greater than 5000m.
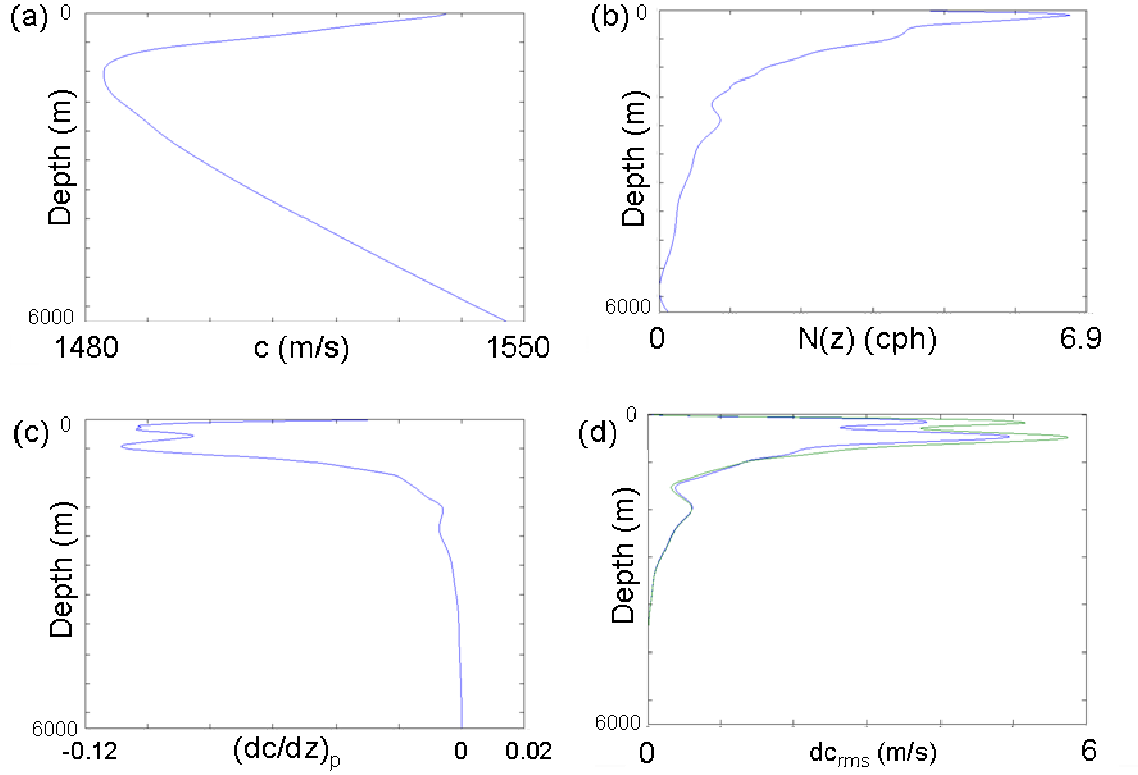
Figure 6.   The background ocean profiles used in this study: (a) sound speed, (b) buoyancy frequency, (c) potential sound speed gradient, (d) RMS sound speed variability. The profiles were derived from the World Ocean Atlas 2001 annual database for 23°N 125°E. In (d), the blue line is the average of 32 random realization of the ocean, while the green line is the theoretical profile for the acoustic model.

2.   Eddies

Eddy-induced sound speed perturbations are a function of the vertical displacement, $\zeta(\vec{r},t)$, of the water column by the eddy:

$$\delta c(\vec{r},t) = \zeta(\vec{r},t)\left(\frac{\partial c}{\partial z}\right)_p .$$
(16)

16

In order to model the vertical displacement caused by the eddies, eddy fields are modeled as a superposition of linear Rossby waves, in accordance with Munk et al. [1995]. This method creates computationally efficient eddy approximations, which are spatially and temporally correct in scale.

This method neglects the non-linear nature of ocean eddies, but provides a first-order approximation of the vertical displacement of the eddy:

$$\zeta(x, y, z, t) = \sum_{j=1}^{j_{max}} \int a_j(k_x, k_y) W_j(z) e^{i(k_x x + k_y y - \sigma_j(k_x, k_y))} dk_x dk_y, \tag{17}$$

where $a_j(k_x, k_y)$ is the Rossby wave amplitude, which is a zero mean Gaussian random variable; $W_j(z)$ is the baroclinic Rossby mode, as depicted in Figure 7; k_x, k_y, and σ are Rossby wavenumbers and frequency; and j_{max} is the maximum Rossby mode number treated. In this study, $j_{max} = 4$, and eddies with wavelengths between 25 and 1100km and frequencies of 0.04 to 3.2 cycles per year were modeled. The spectral form used is:

$$\left\langle \left| a_j(k_x, k_y) \right|^2 \right\rangle = \frac{S_\zeta(k_h)}{2\pi k_h}, \tag{18}$$

where $k_h^2 = k_x^2 + k_y^2$. The normal mode equation is:

$$\frac{d^2 W}{dz^2} + \lambda^2 \frac{N^2(z)}{f^2} W_j = 0 \tag{19}$$

where $\lambda^2 = -\left(k^2 + l^2 + \frac{\beta k}{\sigma} \right)$, N is the buoyancy frequency, and f is the Coriolis parameter.
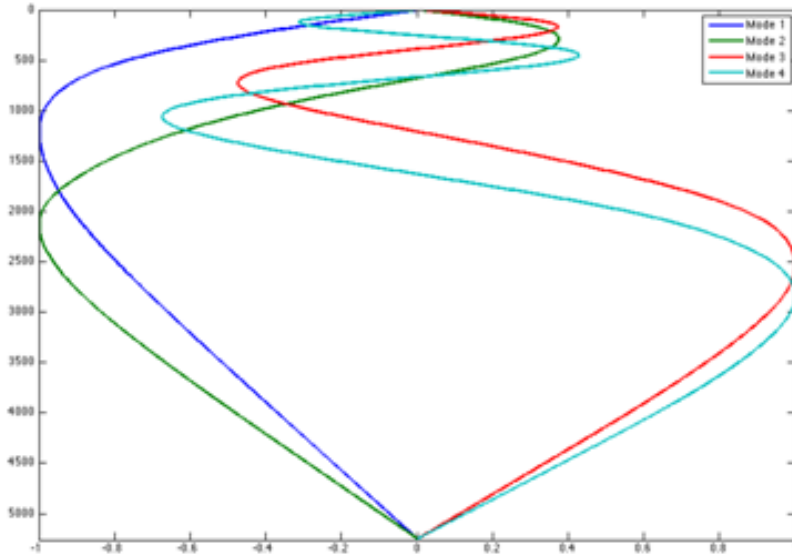
Figure 7.   Normal mode curves.

Based on the findings of Stammer [1997], we assume isotropic variability to facilitate computational efficiency in modeling. As shown in Figure 4, two forms of eddy wavenumber spectra are used: that developed by Stammer [1997] and a Lorentzian form [Munk et al. 1995], both described in Chapter II.

As suggested by Wunsch [1997], we treated 80% of observed surface elevation as due to baroclinic modes, with the baroclinic energy distributed in the first four modes. Therefore, 20% of the total energy was modeled in the barotropic mode, which has no impact on sound speed. The remaining 80% was modeled as baroclinic energy and further partitioned into Mode 1 (70%), Mode 2 (15%), Mode 3 (9%), and Mode 4 (6%).

Based on satellite altimetry, the Philippine Sea has approximately 15 cm root mean square (RMS) variability [Wunsch 1997; Qui 1999], as shown in Figures 8 and 9. The Philippine Sea variability is much greater than most of the eastern North Pacific Ocean, where NPAL experiments have taken place in the past and where RMS variability is approximately 5cm. SSH variability of 15cm RMS was used as a normalization factor, and random eddy fields were created to overlay on the background ocean. Examples of random eddy fields are shown in Figure 10, where (a) is based on the Stammer spectrum

18

and appears to have a correlation length around 150km and (b) is based on the Lorentzian spectrum and has a correlation length around 50km, as determined by the value of k*:

$$L_H \approx k^* \Big/ 2\pi \tag{20}$$
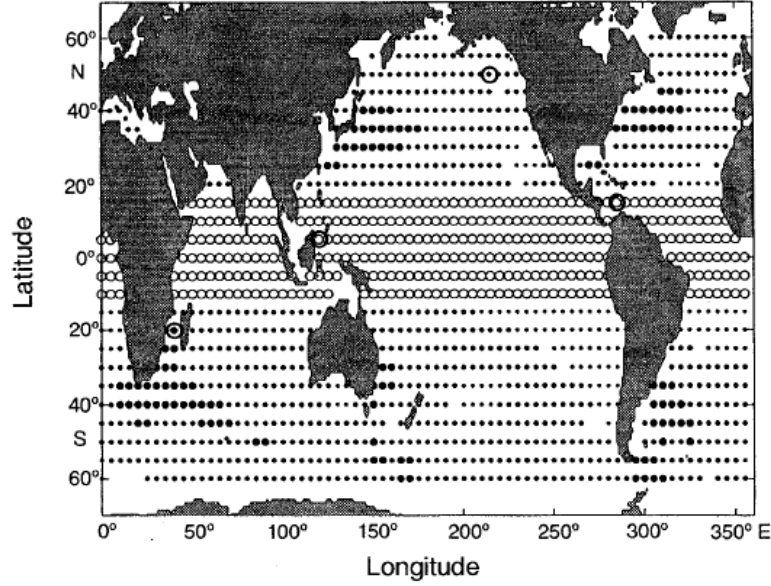
Figure 8. Ocean variability (γ) from TOPEX/Poseidon altimetric data from December 1992 to November 1995, plotted as tropical ocean (open circles), very low energy areas with $\gamma < 6$cm (small dots), the bulk of the oceans with $6\text{cm} < \gamma < 15$cm (medium dots), and the high energy areas with $\gamma > 15$cm. Large bold circles are marked for another purpose and can be ignored here. From Stammer 1997.
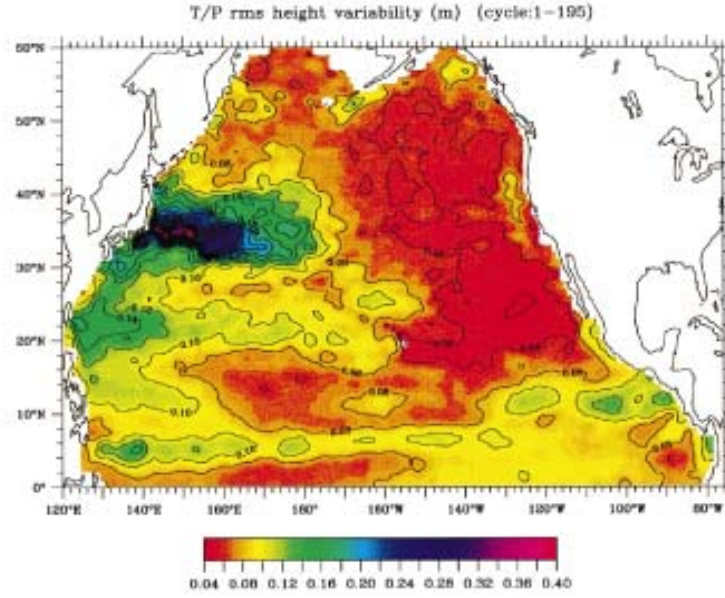
Figure 9.   Map of RMS sea surface height (SSH) variability in the North Pacific Ocean, based on TOPEX/Poseidon data from October 1992 to December 1997. From Qui 1999.
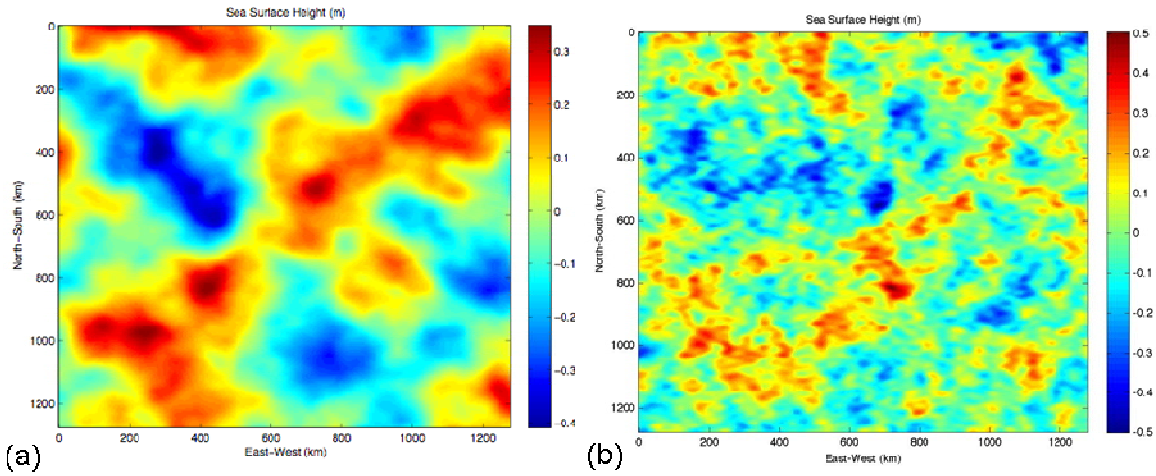
Figure 10.   Map of surface elevation, modeled using the background ocean for 23°N 125°E and random eddy fields from the (a) Stammer spectrum and (b) Lorentzian spectrum.

20

IV. RESULTS AND ANALYSIS

Eight different sets of simulations were run with varying combinations of the following parameters to simulate acoustic transmission through eddy fields: acoustic frequency (20 Hz or 250 Hz), eddy wavenumber spectrum (Stammer or Lorentz), and source depth (50m or 200m), as shown in Table 1. The frequencies used were chosen to represent possible tactically-relevant frequencies; 20Hz is near a blade-rate frequency, and 250Hz is near machinery frequencies, plus it is the frequency to be used in the NPAL experiment. The depths were chosen to simulate depths at which submarines might transit. Each simulation was run for 32 realizations of the ocean, with full water-column transmission loss (TL) diagrams based on the Gaussian sound source (described in Chapter III) for each realization. In addition, full water-column TL diagrams were generated for the unperturbed ocean based on the Gaussian sound source. Single-receiver, point-to-point transmission loss curves from perturbed oceans were averaged and compared to the unperturbed ocean TL curves to assess the effects of ocean mesoscale features on transmission loss.

Table 1.   Eight different combinations of frequency, spectrum, and source depth used to generate TL curves through eddy-field oceans. Each combination was run 32 times.

Run	Frequency	Spectrum	Source Depth
#1	20 Hz	Stammer	50m
#2	20 Hz	Stammer	200m
#3	20 Hz	Lorentz	50m
#4	20 Hz	Lorentz	200m
#5	250 Hz	Stammer	50m
#6	250 Hz	Stammer	200m
#7	250 Hz	Lorentz	50m
#8	250 Hz	Lorentz	200m

A. BACKGROUND OCEAN AND EDDY FIELD TRANSMISSION LOSS

Each of the eight simulations generated one full water-column TL diagram for the unperturbed ocean and 32 plots for the eddy realizations. Examples of each combination are shown in Figures 11-18. The TL diagrams on the left are examples of transmission loss through an unperturbed ocean, while the TL diagrams on the right are examples of transmission loss through a modeled eddy-field. Cold colors indicate areas of high transmission loss, while warm colors indicate lower transmission loss. These TL diagrams do not include cylindrical spreading, and the seafloor is depicted by the red line at 5250m.

Convergence zones are defined as regions in the deep ocean where sound rays, refracted from the depths, return to the surface. The rays are focused at or near the surface in successive intervals [Commander, Navy Warfare Development 2006]. If these intervals are viewed in plan view, they appear as concentric circles around a source, which are referred to as convergence zone (CZ) rings. In the vertical cross-sections shown in Figures 11-18, convergence zones appear as the brighter loops of green, yellow and orange through the entire water column. CZs have horizontal lengths on order 50km, with focusing regions (rings) near the surface. For instance, in Figure 11a, the convergence zone rings are approximately at 60km, 120km, 180km, 250km, 310km, and 370km.

Figures 11-18 demonstrate some of the common physical processes caused by the eddy fields. In all the figures (11-18), there is noticeable vertical and horizontal shifting of the CZs and spreading of CZs. Specifically, Figure 18b is an example of considerable shifting of the CZ, as acoustic rays get refracted at the third CZ ring, near 175km at 500m depth, creating a secondary set of CZ loops and partially filling in the shadow zones (dark blue areas) that existed in the unperturbed case (Figure 18a). To clarify, the CZ rings in 18a are near 65km, 130km, 190km, 250km, 310km, and 375km. In Figure 18b, the first two CZ rings are similar: 60km, 120km, but at the third ring (~175km), acoustic rays from the near-source side of the transmission "beam" are diverted, creating two beams of transmission. The original beam has CZ rings at 250km, 310km, and 380km, while the newly created beam has CZ rings at 210km, 260km, 325km, and 385km.

In a few cases, the eddy fields alter TL by driving energy into the seafloor (as shown in 15b) and even into the surface duct (as in Figures 13b, 14b, and 17b). Energy driven into the seafloor causes significantly damped transmission after the interaction, indicated by darker blue colors in the TL plot. For example, in Figure 15b, the first bottom interaction is around 35km, after which there is less turquoise and more of the darker blues, indicating increased transmission loss as compared to the unperturbed simulation (Figure 15a). Energy trapped in surface ducts is depicted by a yellow or green horizontal line of energy near the surface, for example in Figure 13b from the origin to 150km. In Figure 14b, this occurs at the fourth and fifth CZ rings, about 250km and 325km; trapping is evident in Figure 17b near 250km. Scintillation is quantified by the varying intensities between realizations, so its effects are not depicted in these figures.

Figure 11.   (a) Full water-column transmission loss diagram for unperturbed ocean: frequency 20 Hz, source depth 50m. (b) As in (a), but with ocean perturbed by Stammer eddy field. In (b), the eddy field causes spreading and shifting of the CZs.

Figure 12.   (a) Full water-column transmission loss diagram for unperturbed ocean: frequency 20 Hz, source depth 200m. (b) As in (a), but with ocean perturbed by Stammer eddy field. In (b), the eddy field causes spreading and shifting of the CZs.
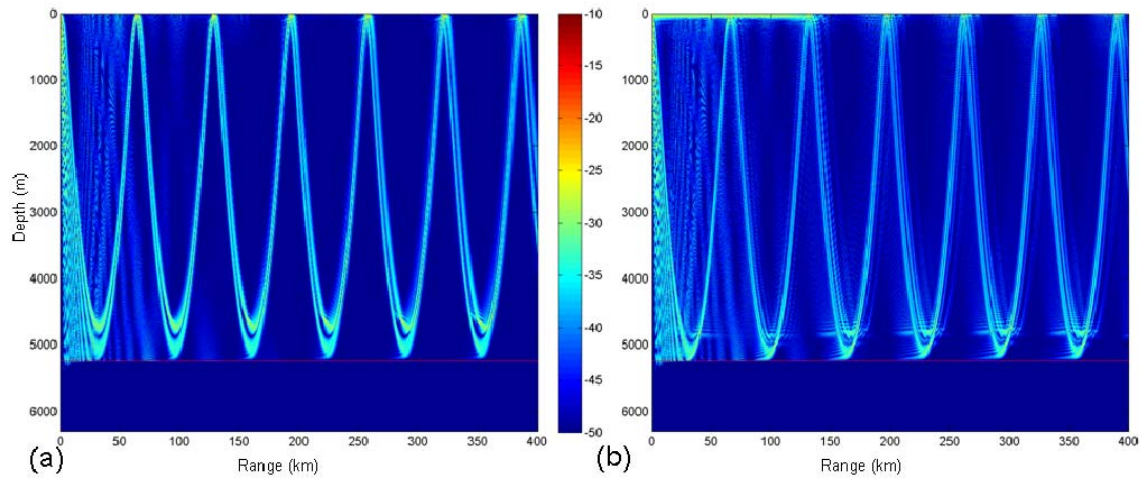
Figure 13.   (a) Full water-column transmission loss diagram for unperturbed ocean: frequency 250 Hz, source depth 50m. (b) As in (a), but with ocean perturbed by Stammer eddy field. In (b), the eddy field causes energy to become trapped in the surface duct near the origin. There is also spreading and shifting of the CZs created by energy that escapes the surface duct.
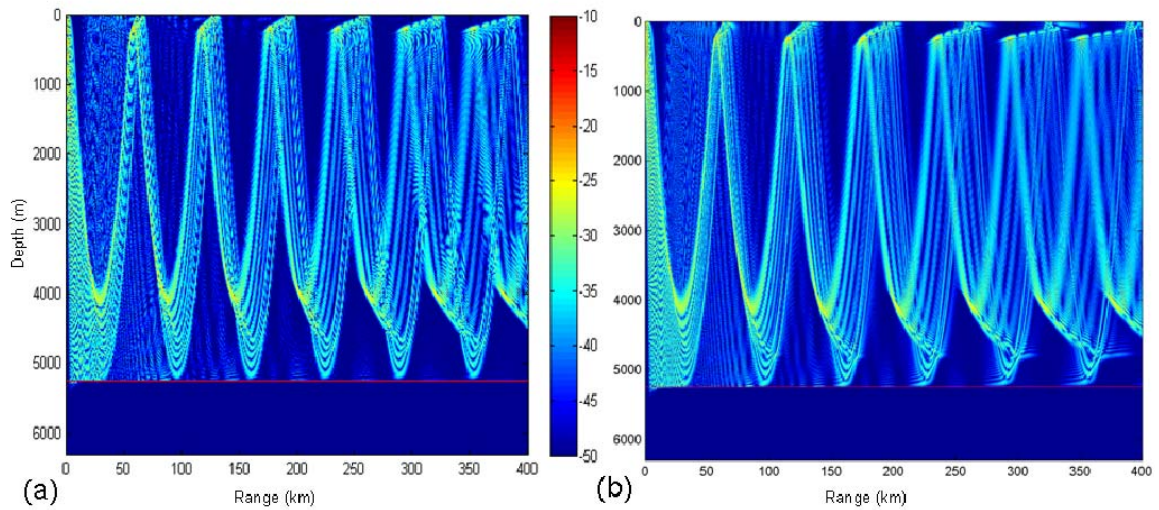
Figure 14.   (a) Full water-column transmission loss diagram for unperturbed ocean: frequency 250 Hz, source depth 200m. (b) As in (a), but with ocean perturbed by Stammer eddy field. In (b), the eddy field causes spreading and shifting of the CZs, as well as some trapped energy in the surface duct near 250 and 325 km.

25
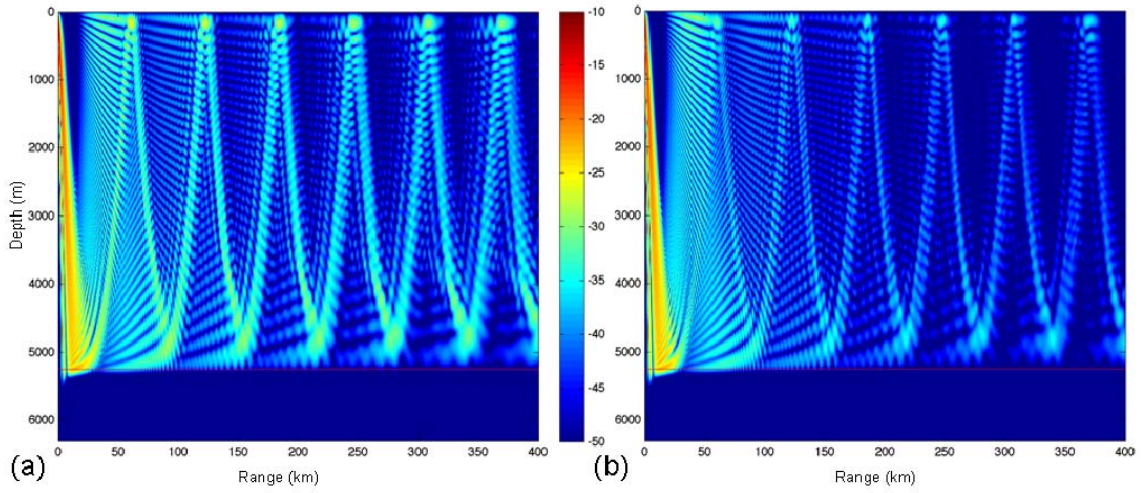
Figure 15.   (a) Full water-column transmission loss diagram for unperturbed ocean: frequency 20 Hz, source depth 50m. (b) As in (a), but with ocean perturbed by Lorentz eddy field. In (b), the eddy field causes significant energy to be trapped in the seafloor, as shown by the darker blue colors in (b), especially after the first bottom interaction around 35km. The eddy field also causes spreading and shifting of the CZs.
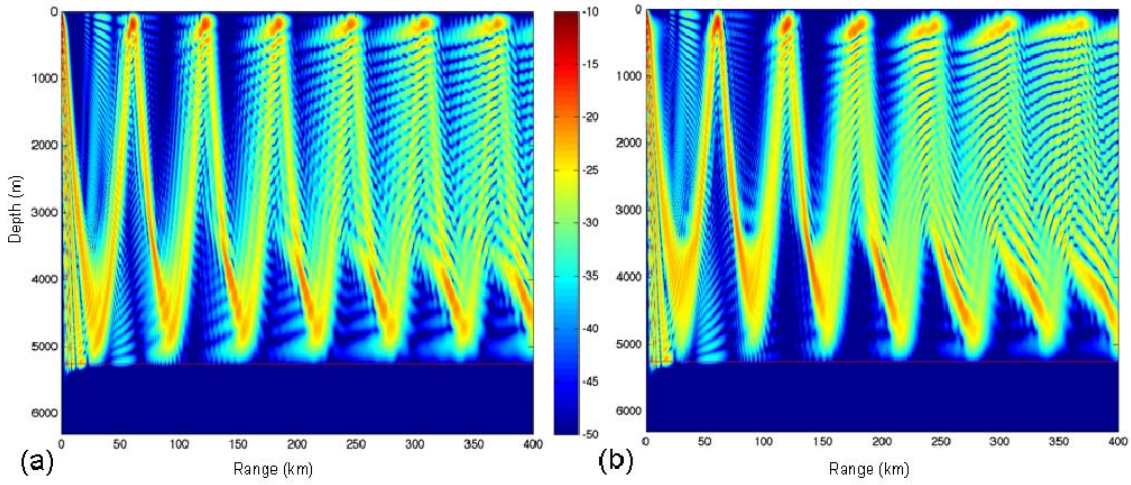
Figure 16.   (a) Full water-column transmission loss diagram for unperturbed ocean: frequency 20 Hz, source depth 200m. (b) As in (a), but with ocean perturbed by Lorentz eddy field. In (b), the eddy field causes spreading and shifting of the CZs.
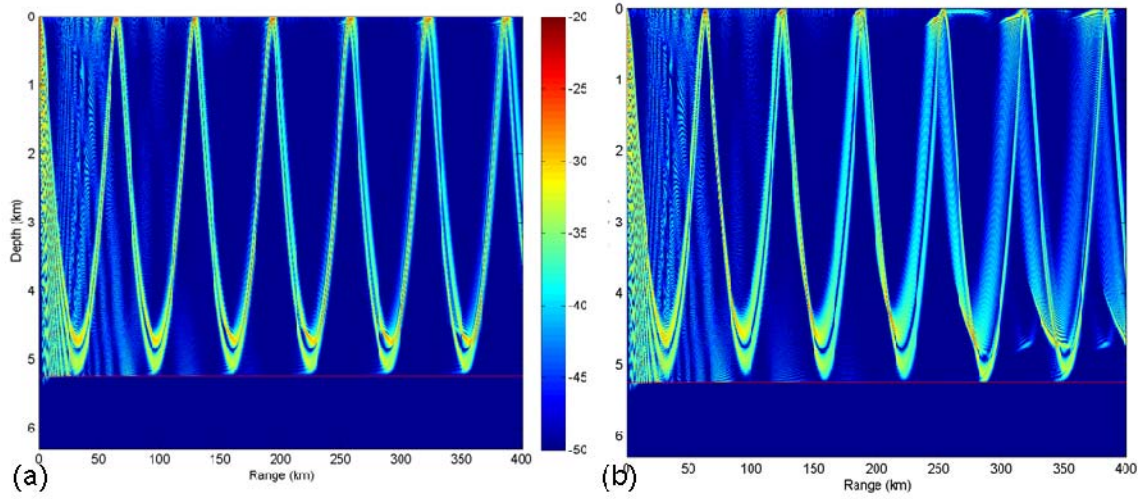
Figure 17.   (a) Full water-column transmission loss diagram for unperturbed ocean: frequency 250 Hz, source depth 50m. (b) As in (a), but with ocean perturbed by Lorentz eddy field. In (b), the eddy field causes energy to be trapped in the surface duct around 250 km, as well as spreading and shifting of the CZs.

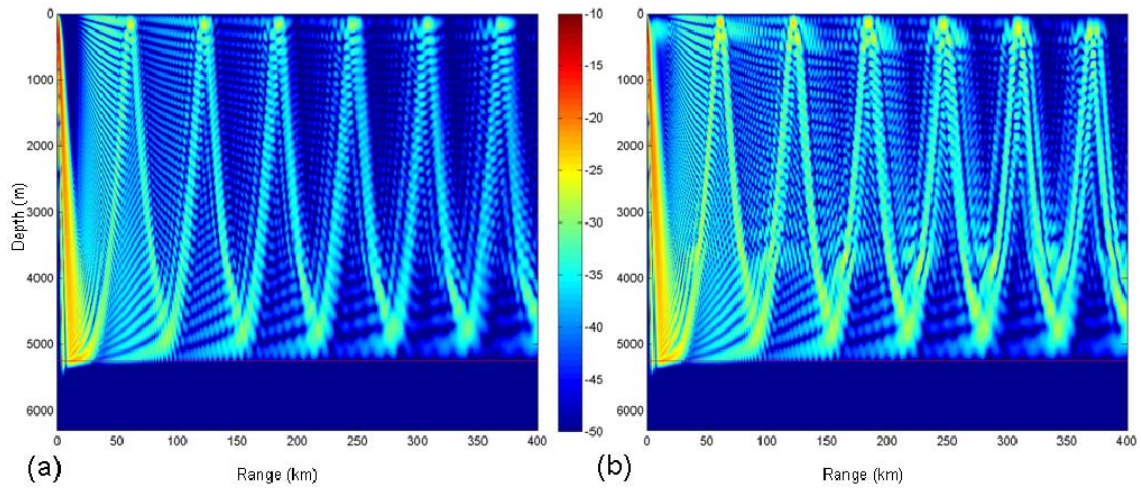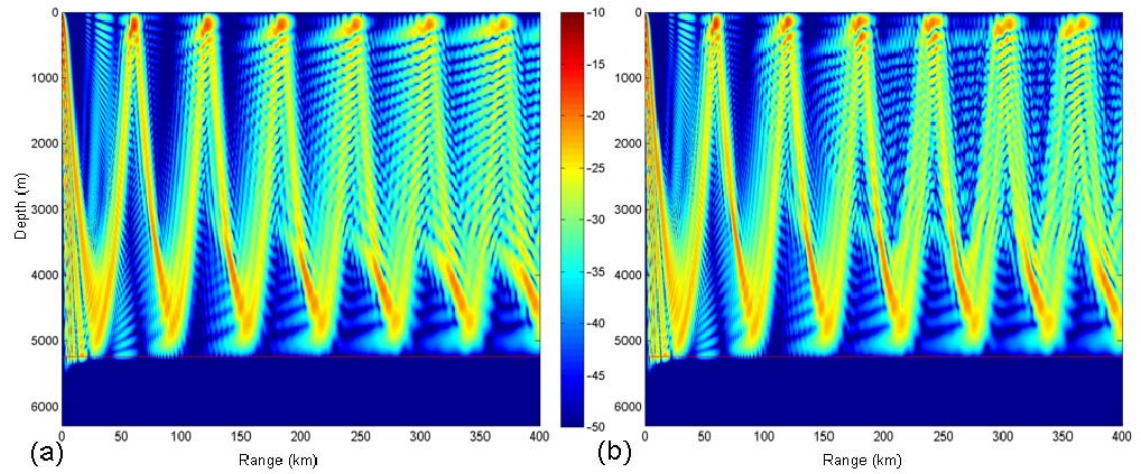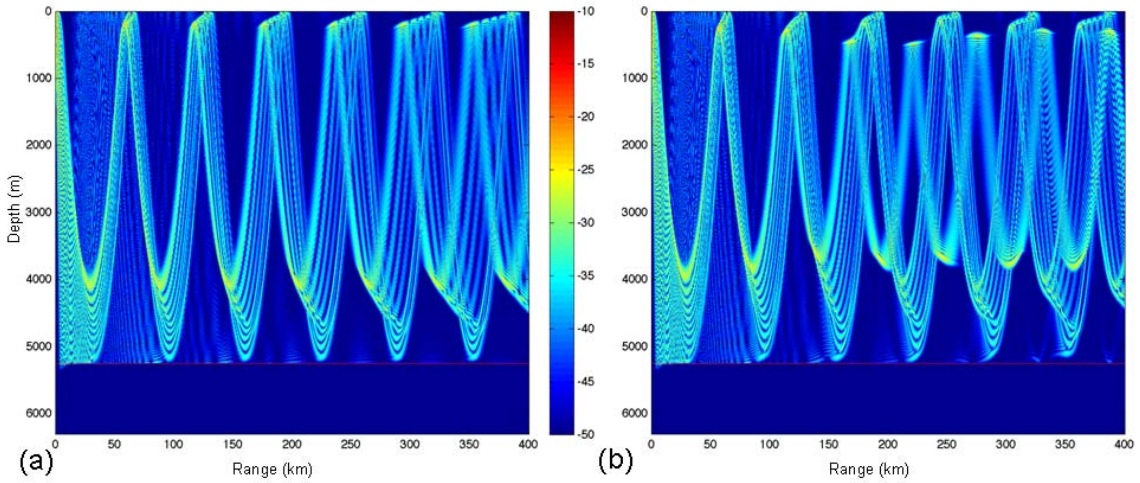Figure 18.   (a) Full water-column transmission loss diagram for unperturbed ocean: frequency 250 Hz, source depth 200m. (b) As in (a), but with ocean perturbed by Lorentz eddy field. In (b), the eddy field causes significant spreading and shifting of the CZ energy, which partially fills the shadow zones. The major deviation between the unperturbed and the eddy realization occurs around 175km at about 500m depth in (b).

A quick visual examination of the figures above reveals differences in the CZ structures for high and low frequency sources. Focusing on the unperturbed plots, two distinct processes are causing the different structures visible in Figures 11a-18a. The first is evanescent waves, which cause striations of TL in the shadow zones. For the 20Hz source, the evanescent waves decay more slowly, leaving more energy (brighter colors) in the shadow zones. For the 250Hz source, these evanescent waves decay much more rapidly, so the shadow zones are predominantly free of acoustic energy [Flatté 1979]. Secondly, the lower frequency acoustic energy is more affected by diffraction, leading to much more diffuse and broadened convergence zone loops [Flatté 1979]. This is especially evident in comparing Figures 11a and 13a. The convergence zone loops for the higher frequency (Figure 13a) are much more distinct because they are less affected by diffraction and the associated evanescent waves decay more quickly. Also, the higher frequency source is better focused near the surface, creating more distinct CZ rings [Flatté 1979].

Additionally, the lower frequency has a longer wavelength, so it has a larger-scale interference pattern, which leads to fewer interference bands or lobes in the convergence zone loops [Flatté 1979]. This is especially evident with the deeper source depth. Comparing Figures 12a and 14a, the interference lobes for the lower frequency source are not detectable, while in Figure 14a, at least nine lobes are visually identifiable.

B.   EFFECTS ON TRANSMISSION LOSS

For each of the eight model runs, point-to-point transmission loss curves to a single receiver at 50m depth were calculated for the unperturbed ocean ($\Phi_0(r)$) and for each realization of the eddy fields ($\Phi_i(r)$, where i is the realization number). The TL curves were smoothed with range using a Butterworth filter in order to eliminate the high variability associated with multipath interference patterns. The smoothing serves to eliminate the small-scale shifts from the interference pattern and to focus statistics on the large-scale changes in intensity. The smoothing process is equivalent to averaging over range, which is algebraically similar to averaging over frequency, so smoothing these curves makes them equivalent to TL curves one might see with a broadband signal

[Harrison and Harrison 1995]. Hence, even though single frequencies are modeled, the results presented here are reasonable estimations what might occur during the NPAL experiment where broadband signals will be used.
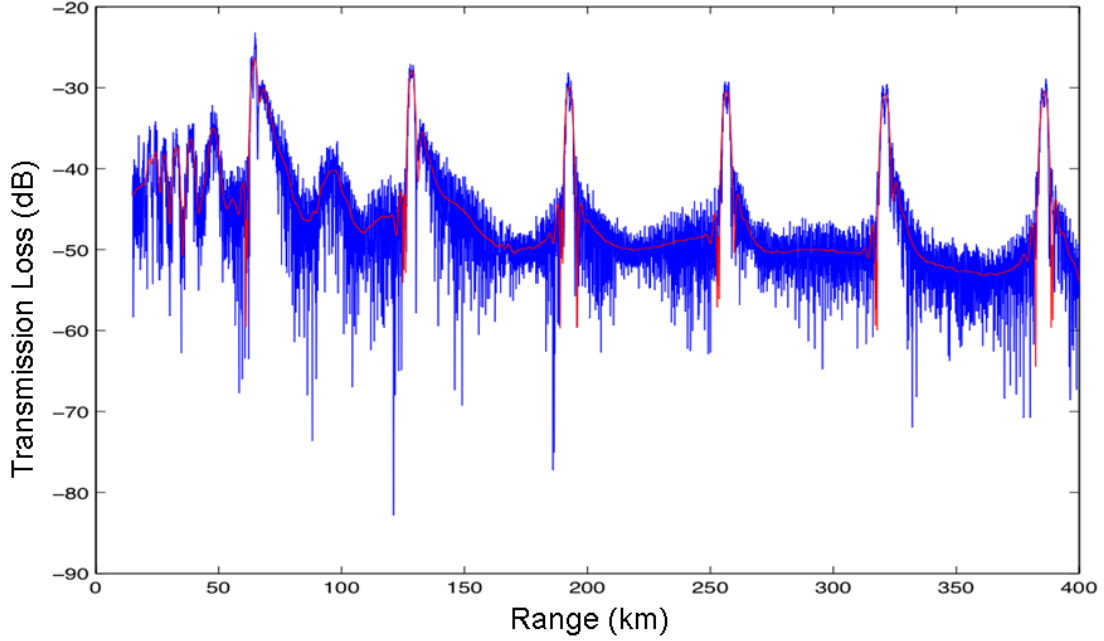
Figure 19.　　　An example of unsmoothed TL curve (blue) showing much variability due to multipath interference. The red curve is smoothed using the Butterworth filter.

After smoothing, the 32 curves from each run were averaged with each other to create a composite eddy TL curve for each scenario:

$$\Phi_E(r) = 10\log_{10}\left(\frac{1}{32}\sum_{i}^{i=32} I_i(r)\right),\tag{21}$$

where Φ_E is the composite eddy-induced transmission loss in dB and $I_i(r)$ is the acoustic intensity at range r for each realization i. These composite curves were then differenced with the unperturbed ocean curve

$$\Phi_b(r) = \Phi_E(r) - 10\log 10(I_0(r)),\tag{22}$$

where $\Phi_b(r)$ is the bias curve and $I_0(r)$ is the unperturbed acoustic intensity at range r. The $\Phi_b(r)$ curves are presented below in Figures 20-32 as the top panel in (a) and (b) and represent the expected increase or decrease of acoustic intensity through an eddy field.

Root mean square variability for the 32 perturbed curves was calculated using the composite eddy TL curve as the mean:

$$\Phi_{RMS}(r) = \sqrt{\left(\frac{1}{32}\sum_i^{i=32} \iota^2(r,i)\right) - \left(\frac{1}{32}\sum_i^{i=32} \iota(r,i)\right)^2} \tag{23}$$

where $\iota_{dB}(r,i) = 10\log_{10}I(r,i)$. $\Phi_{RMS}(r)$ represents the possible variability of sound intensity around the mean TL curve; it is depicted in the bottom panel of Figures 20-32 in (a) and (b).

In order to draw valid summary statistics from these two curves ($\Phi_b(r)$ and $\Phi_{RMS}(r)$), a threshold value above a reasonable ambient noise level was set for each unperturbed TL curve. This created an index array of all range positions that were above the threshold value. The Φ_b and Φ_{RMS} values associated with this index were used to calculate the summary statistics. This method emphasizes the regions where acoustic energy is significant, which are also regions of high variability, and eliminates TL bias and variability where the sound level would be too low to be detectable.

The summary statistics used to analyze the trends among the three variables are significant bias (Φ_b), which is a quantification of the shift in detectable sound caused by the eddy field; and significant RMS (Φ_{RMS}), which is a measure of the variability of sound through the eddy field. Φ_b takes into account three of the mechanisms by which eddies alter TL – shifting CZs, driving energy into the seafloor, and trapping energy in a surface duct. Φ_{RMS} incorporates the fourth mechanism – scintillation. Summary statistics are presented in Table 2, and they will be discussed further in the paragraphs 1-3 below.

Expected uncertainties for individual estimates of $\Phi_b(r)$ and $\Phi_{RMS}(r)$ are of the order $1/\sqrt{32}$ or about 17%; however, range averaging to obtain the significant summary statistics reduces this error by about a factor 2. Therefore, the uncertainty or error associated with the summary statistics is about 8%. This becomes important when discussing the significance of Φ_b and Φ_{RMS} values.

30

Table 2.   Summary statistics: Φ_b is a measure of the expected decibel shift of acoustic energy through an eddy ocean versus the unperturbed case (measured only where the signal has high intensity above the given threshold). Φ_{RMS} is the square-root of significant variance, a measure of the variance of the 32 realizations around their mean (calculated for above-threshold signal).

Run	Freq (Hz), Spectra, Source Depth (m)	Φ_b (dB)	Φ_{RMS} (dB)
#1	20, Stammer, 50	0.59	2.17
#2	20, Stammer, 200	0.80	3.33
#3	20, Lorentz, 50	0.59	2.36
#4	20, Lorentz, 200	0.88	3.02
#5	250, Stammer, 50	5.33	6.18
#6	250, Stammer, 200	5.69	6.58
#7	250, Lorentz, 50	4.37	5.50
#8	250, Lorentz, 200	5.46	5.66

1.   Frequency Dependency

For each frequency, four combinations of spectra and source depth were computed, as shown in Table 1, which allows for four comparisons of frequency tendencies on transmission loss. Figures 20 through 23 show these comparisons, where the top two panels are $\Phi_b(r)$, and the bottom two panels show $\Phi_{RMS}(r)$. The plots on the left are for the 20Hz source (a), and the plots on the right are for the 250Hz source (b). Summary statistics are shown in Table 2, and Table 3 is a comparison of the statistics for the two different frequencies modeled.

Figure 20.　　(a) $\Phi_b(r)$ and $\Phi_{RMS}(r)$, using Stammer spectrum, frequency 20 Hz, source depth 50m, receiver depth 50m.　Statistics for run #1 show Φ_b=0.59dB and Φ_{RMS}=2.17dB.　(b) As in (a), but with frequency 250 Hz.　Statistics for run #5 show Φ_b=5.33dB and Φ_{RMS}=6.18dB.

Figure 21.　　(a) $\Phi_b(r)$ and $\Phi_{RMS}(r)$, using Stammer spectrum, frequency 20 Hz, source depth 200m, receiver depth 50m.　Statistics for run #2 show Φ_b=0.80dB and Φ_{RMS}=3.33dB.　(b) As in (a), but with frequency 250 Hz.　Statistics for run #6 show Φ_b=5.69dB and Φ_{RMS}=6.58dB.

Figure 22.   (a) $\Phi_b(r)$ and $\Phi_{RMS}(r)$, using Lorentzian spectrum, frequency 20 Hz, source depth 50m, receiver depth 50m. Statistics for run #3 show Φ_b =0.59dB and Φ_{RMS} =2.36dB. (b) As in (a), but with frequency 250 Hz. Statistics for run #7 show Φ_b =4.37dB and Φ_{RMS} =5.50dB.

Figure 23.   (a) $\Phi_b(r)$ and $\Phi_{RMS}(r)$, using Lorentzian spectrum, frequency 20 Hz, source depth 200m, receiver depth 50m. Statistics for run #4 show Φ_b =0.88dB and Φ_{RMS} =3.02dB. (b) As in (a), but with frequency 250 Hz. Statistics for run #8 show Φ_b =5.46dB and Φ_{RMS} =5.66dB.

Table 3.   Comparison of statistics for low frequency (20Hz) transmissions versus higher frequency (250Hz) transmissions through the modeled eddy fields. Consistently, the acoustic energy from the higher frequency source experienced more Φ_b and Φ_{RMS} than the low frequency acoustic energy.

Run	Freq (Hz), Spectra, Source Depth (m)	Φ_b (dB)	Φ_{RMS} (dB)	Run	Freq (Hz), Spectra, Source Depth (m)	Φ_b (dB)	Φ_{RMS} (dB)
#1	20, Stammer, 50	0.59	2.17	#5	250, Stammer, 50	5.33	6.18
#2	20, Stammer, 200	0.80	3.33	#6	250, Stammer, 200	5.69	6.58
#3	20, Lorentz, 50	0.59	2.36	#7	250, Lorentz, 50	4.37	5.50
#4	20, Lorentz, 200	0.88	3.02	#8	250, Lorentz, 200	5.46	5.66

Figures 20-23 and Table 3 show that Φ_b values for 20Hz are less than one decibel, while the corresponding values for 250Hz are about five decibels. This result is somewhat expected because lower frequencies are more stable, and the acoustic energy is not as affected by mesoscale features as the higher frequency energy. For the higher frequency, there is more energy refracted into the shadow zones, which allows detectable acoustic energy where there previously had been none. The lower frequency energy also was not as susceptible to refraction and trapping in the surface duct because the lower acoustic frequencies have longer wavelengths which are not trapped as easily in the surface layer.

From Figures 20-23 and Table 3, the Φ_{RMS} values for 20Hz are two to three decibels, and the corresponding values for 250Hz are five to six decibels. This result was also expected due to greater stability of the low frequency signal. The variability measurement is a quantification of scintillation occurring, which is caused by multipath interference. The high frequency signal is more likely to break into micro-rays, which are the primary source of multipath interference.

Tactically, this dependence on frequency indicates that less variability is expected with low frequency sources. In other words, acoustic prediction for low frequency tones does not require mesoscale features for accurate ranges.

34

2. Dependency on Spectrum

For each spectrum, four combinations of frequency and source depth were computed, as shown in Table 1, which allows for four comparisons of spectral effects on transmission loss. Figures 24 through 27 show these comparisons, with the top two panels being $\Phi_b(r)$, and the bottom two panels showing $\Phi_{RMS}(r)$. The plots on the left are for the Stammer eddy spectrum (a), and the plots on the right are for the Lorentzian eddy spectrum (b). The Stammer spectrum has correlation lengths around 150km, while the Lorentzian spectrum has correlation lengths around 50km. Summary statistics are shown in Table 2, and a side-by-side comparison of the statistics for the two spectral cases is shown in Table 4.
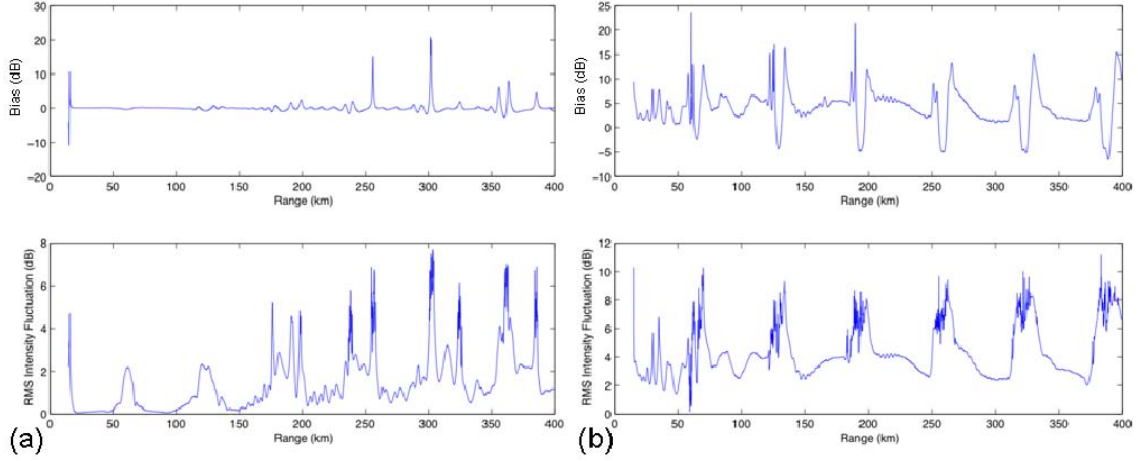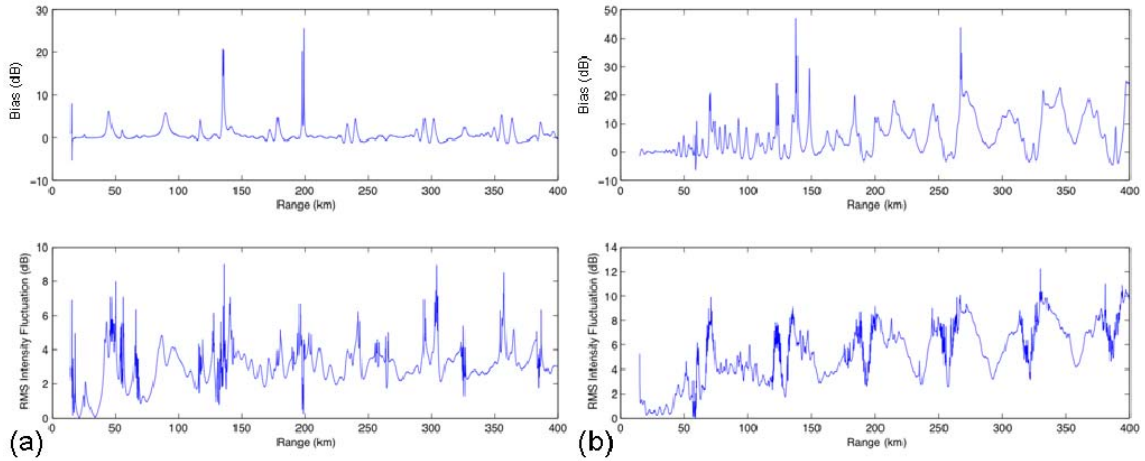

Figure 24.   (a) $\Phi_b(r)$ and $\Phi_{RMS}(r)$, using Stammer spectrum, frequency 20 Hz, source depth 50m, receiver depth 50m. Statistics for run #1 show Φ_b=0.59dB and Φ_{RMS}=2.17dB. (b) As in (a), but with Lorentzian spectrum. Statistics for run #3 show Φ_b=0.59dB and Φ_{RMS}=2.36dB.
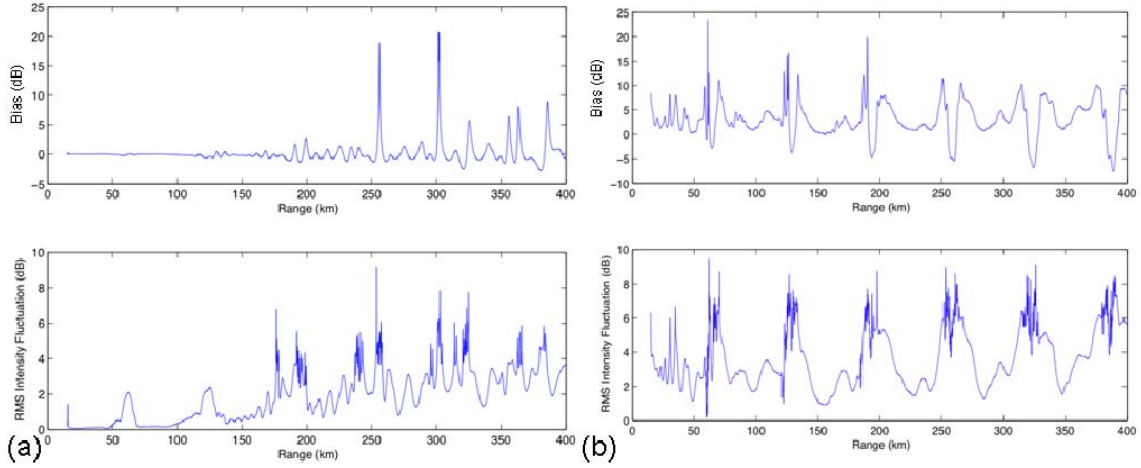
Figure 25.   (a) $\Phi_b(r)$ and $\Phi_{RMS}(r)$, using Stammer spectrum, frequency 20 Hz, source depth 200m, receiver depth 50m. Statistics for run #2 show Φ_b=0.80dB and Φ_{RMS}=3.33dB. (b) As in (a), but with Lorentzian spectrum. Statistics for run #4 show Φ_b=0.88dB and Φ_{RMS}=3.02dB.
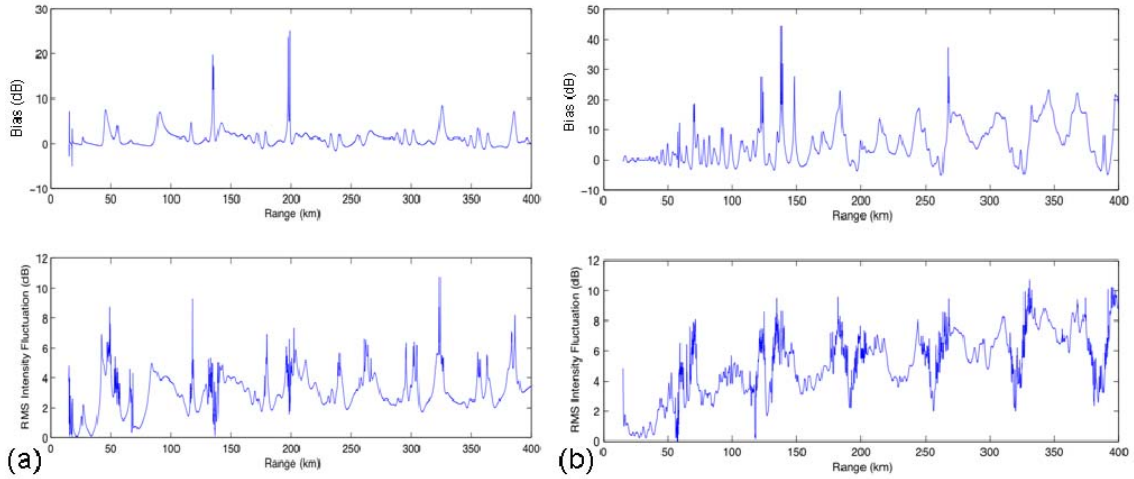

Figure 26.   (a) $\Phi_b(r)$ and $\Phi_{RMS}(r)$, using Stammer spectrum, frequency 250 Hz, source depth 50m, receiver depth 50m. Statistics for run #5 show Φ_b=5.33dB and Φ_{RMS}=6.18dB. (b) As in (a), but with Lorentzian spectrum. Statistics for run #7 show Φ_b=4.37dB and Φ_{RMS}=5.50dB.

36

Figure 27.   (a) $\Phi_b(r)$ and $\Phi_{RMS}(r)$, using Stammer spectrum, frequency 250 Hz, source depth 200m, receiver depth 50m. Statistics for run #6 show Φ_b =5.69dB and Φ_{RMS} =6.58dB. (b) As in (a), but with Lorentzian spectrum. Statistics for run #8 show Φ_b =5.46dB and Φ_{RMS} =5.66dB.

Table 4.   Comparison of statistics for Stammer spectrum versus Lorentzian spectrum for the modeled eddy fields. The two spectra produce similar numbers for Φ_b and Φ_{RMS} in all combinations of variables.

Run	Freq (Hz), Spectra, Source Depth (m)	Φ_b (dB)	Φ_{RMS} (dB)	Run	Freq (Hz), Spectra, Source Depth (m)	Φ_b (dB)	Φ_{RMS} (dB)
#1	20, Stammer, 50	0.59	2.17	#3	20, Lorentz, 50	0.59	2.36
#2	20, Stammer, 200	0.80	3.33	#4	20, Lorentz, 200	0.88	3.02
#5	250, Stammer, 50	5.33	6.18	#7	250, Lorentz, 50	4.37	5.50
#6	250, Stammer, 200	5.69	6.58	#8	250, Lorentz, 200	5.46	5.66

Figures 24-27 and Table 4 show that Φ_b values for both Stammer and Lorentzian eddies are less than one decibel for the low frequency case, with the difference between corresponding cases for the two spectra being only a few tenths of a decibel. For the higher frequency examples, the two spectra cause similar values for Φ_b, right around five decibels for both spectra. Based on expected uncertainties for Φ_b, a few tenths of a decibel is not a significant difference. An insignificant trend between the two spectra is a surprising result considering how different the sea surface height realizations looked (Figure 10). The correlation length for the Lorentzian eddies is approximately 50km, and

the correlation length for the Stammer eddies appears to be approximately 150km, yet these seem to have little to do with the changes in acoustic transmission.

From Figures 24-27 and Table 4, the Φ_{RMS} values for both Stammer and Lorentzian eddies are two to three decibels at the low frequency and five to six decibels at the higher frequency. Again, based on expected uncertainties for Φ_{RMS}, these results are not a significant difference. The results suggest that the eddy wavenumber spectrum has little effect on the acoustic transmissions. Cornuelle and Howe's research [1987] revealed that loop resonance structure and scales are important for travel time variance, yet this study suggests that intensity and arrival time are sensitive to different scales. Until the issue of intensity sensitivity is better resolved, tactical decisions about model resolution cannot accurately be made.

3.   Source Depth Dependency

For each source depth, four combinations of spectra and frequency were computed, as shown in Table 1, which allows for four comparisons of source depth tendencies on transmission loss. Figures 28 through 31 show these comparisons, with the top two panels being Φ_b, and the bottom two panels showing Φ_{RMS}. The plots on the left are for the source at 50m (a), and the plots on the right are for the source at 200m (b). Summary statistics are shown in Table 2, and Table 5 is a comparison of the statistics for the two source depths.
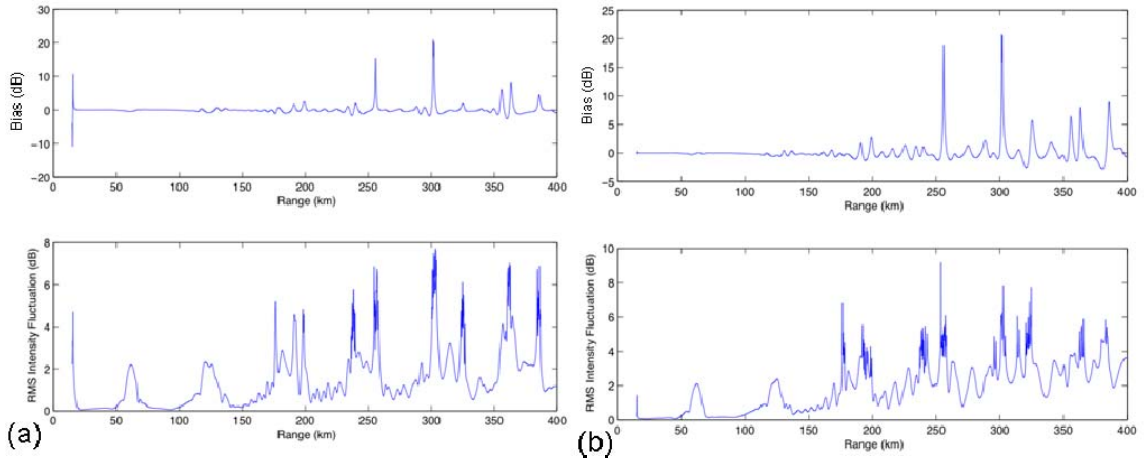
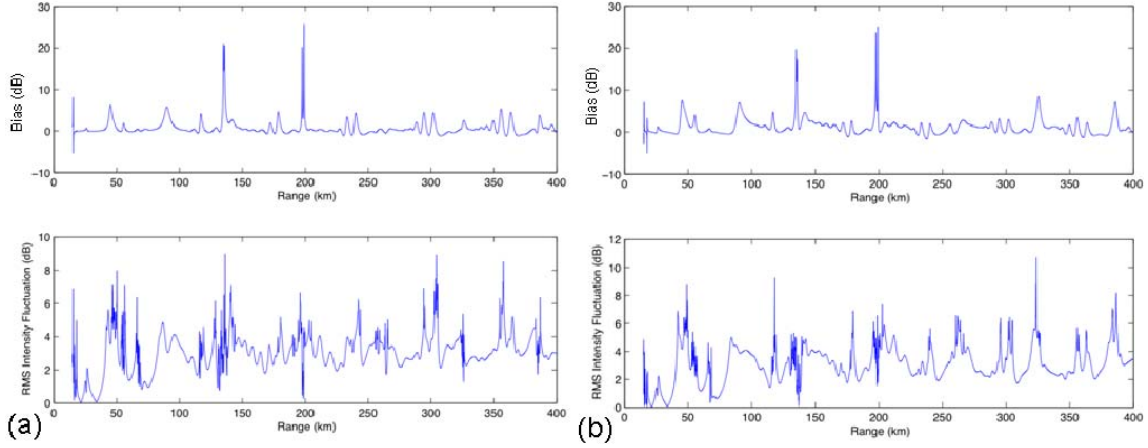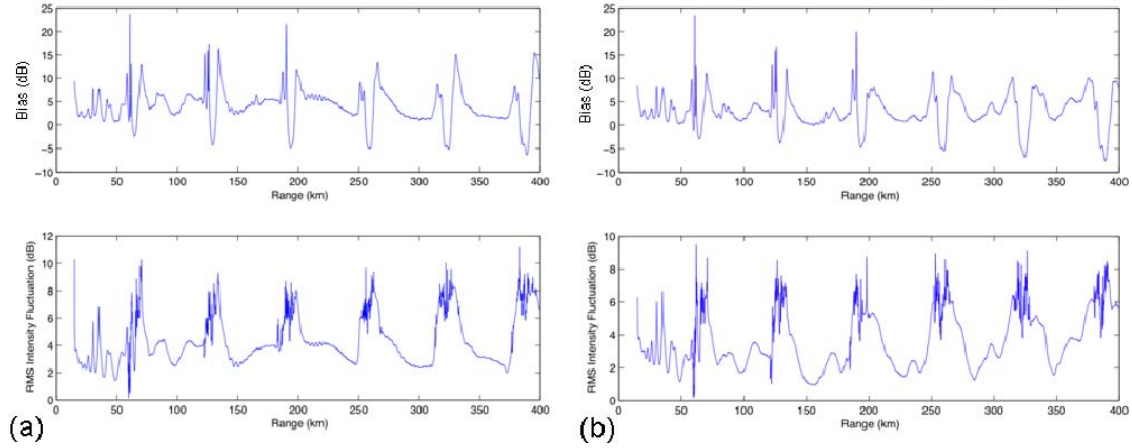Figure 28.   (a) $\Phi_b(r)$ and $\Phi_{RMS}(r)$, using Stammer spectrum, frequency 20 Hz, source depth 50m, receiver depth 50m. Statistics for run #1 show Φ_b =0.59dB and Φ_{RMS} =2.17dB. (b) As in (a), but with source depth 200m. Statistics for run #2 show Φ_b =0.80dB and Φ_{RMS} =3.33dB.

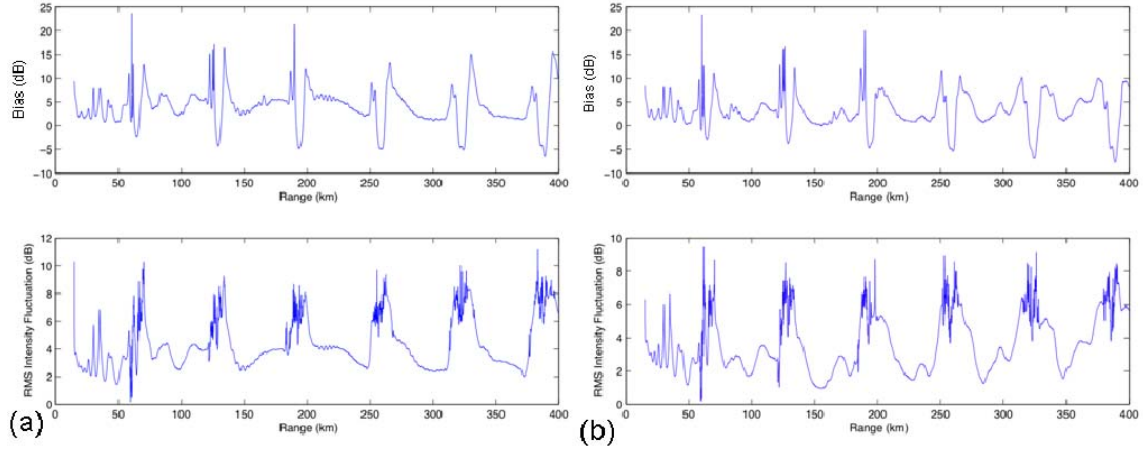Figure 29.   (a) $\Phi_b(r)$ and $\Phi_{RMS}(r)$, using Stammer spectrum, frequency 250 Hz, source depth 50m, receiver depth 50m. Statistics for run #5 show Φ_b =5.33dB and Φ_{RMS} =6.18dB. (b) As in (a), but with source depth 200m. Statistics for run #6 show Φ_b =5.69dB and Φ_{RMS} =6.58dB.
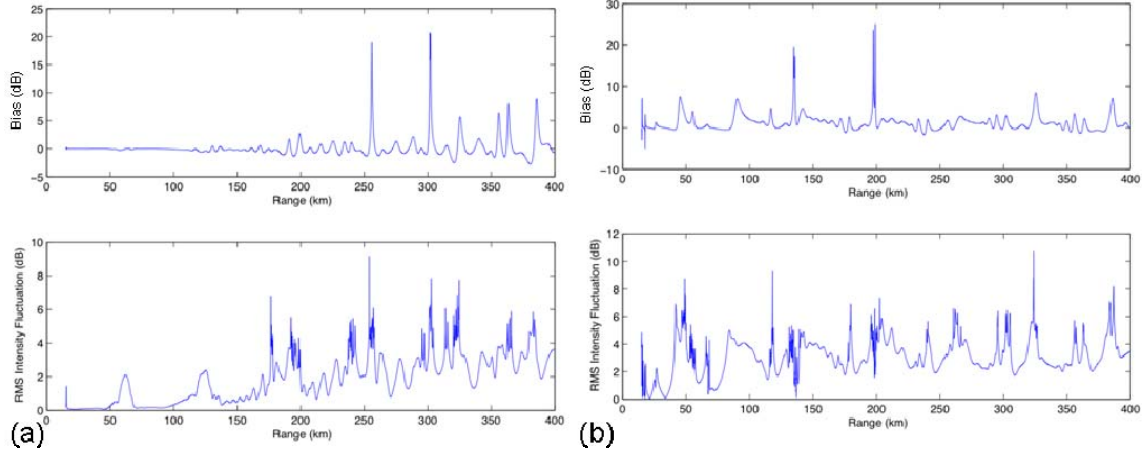
Figure 30. (a) $\Phi_b(r)$ and $\Phi_{RMS}(r)$, using Lorentzian spectrum, frequency 20 Hz, source depth 50m, receiver depth 50m. Statistics for run #3 show Φ_b=0.59dB and Φ_{RMS}=2.36dB. (b) As in (a), but with source depth 200m. Statistics for run #4 show Φ_b=0.88dB and Φ_{RMS}=3.02dB.
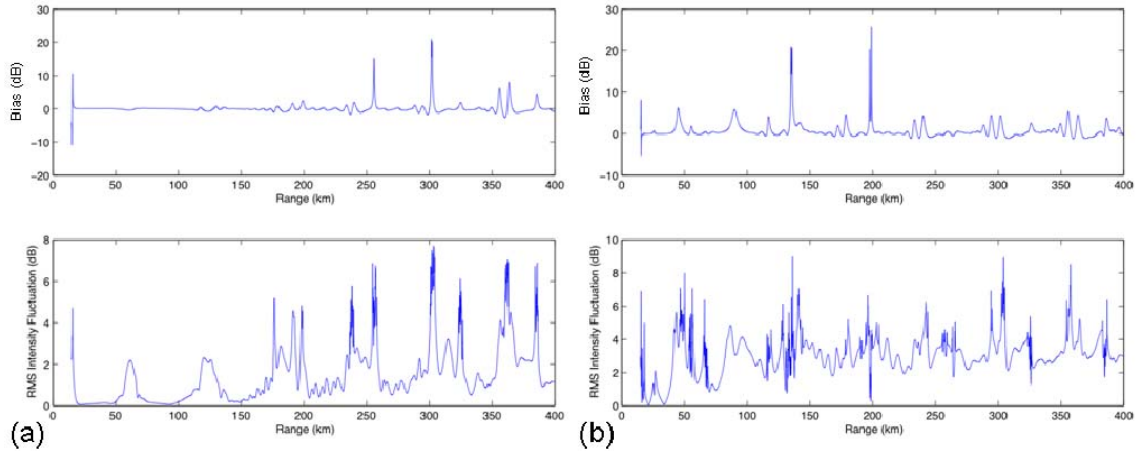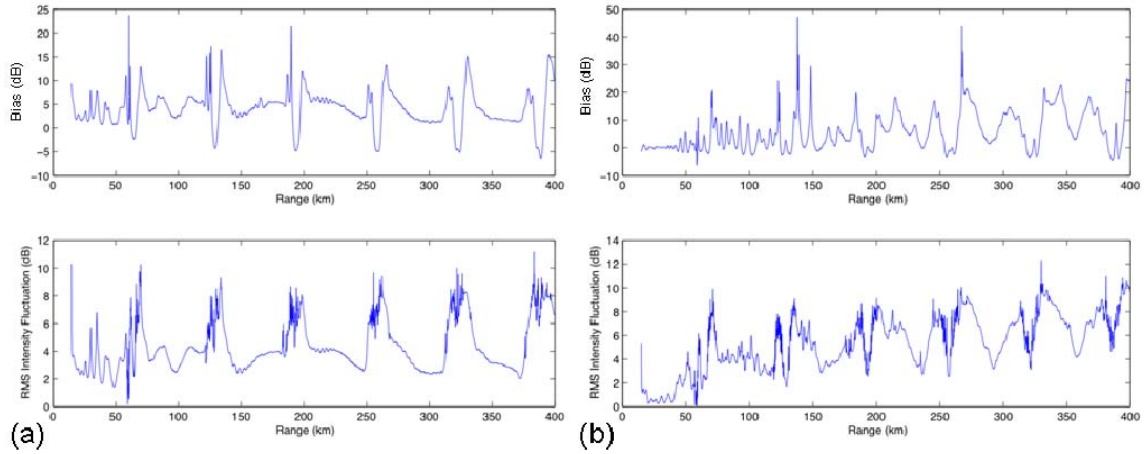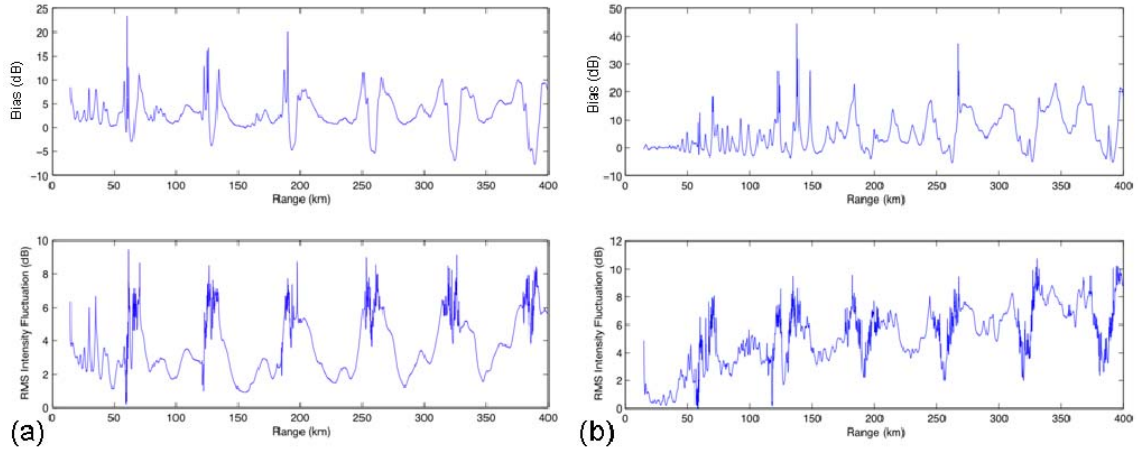

Figure 31. (a) $\Phi_b(r)$ and $\Phi_{RMS}(r)$, using Lorentzian spectrum, frequency 250 Hz, source depth 50m, receiver depth 50m. Statistics for run #7 show Φ_b=4.37dB and Φ_{RMS}=5.50dB. (b) As in (a), but with source depth 200m. Statistics for run #8 show Φ_b=5.46dB and Φ_{RMS}=5.66dB.

Table 5.　　　Comparison of statistics for shallow source depth (50m) versus deeper source depth (200m) through the modeled eddy fields. The depths produce similar orders of magnitude for Φ_b and Φ_{RMS} in all combinations of variables, but the deeper source depth consistently has slightly higher values for both Φ_b and Φ_{RMS}.

Run	Freq (Hz), Spectra, Source Depth (m)	Φ_b (dB)	Φ_{RMS} (dB)	Run	Freq (Hz), Spectra, Source Depth (m)	Φ_b (dB)	Φ_{RMS} (dB)
#1	20, Stammer, 50	0.59	2.17	**#2**	20, Stammer, 200	0.80	3.33
#3	20, Lorentz, 50	0.59	2.36	**#4**	20, Lorentz, 200	0.88	3.02
#5	250, Stammer, 50	5.33	6.18	**#6**	250, Stammer, 200	5.69	6.58
#7	250, Lorentz, 50	4.37	5.50	**#8**	250, Lorentz, 200	5.46	5.66

Figures 28-31 and Table 5 show that Φ_b values for the 50m source are about six tenths of a decibel for the low frequency case and are between four and five decibels for the high frequency case. With the 200m source, the Φ_b values for the low frequency case are just under one decibel with the high frequency case experiencing greater than five decibels Φ_b. The source at 200m consistently has higher values for Φ_b, regardless of frequency. Again, the expected uncertainty in this calculation is about 8%, so these differences in Φ_b are more significant than the uncertainty. Two physical processes are influencing this bias: bottom interaction is causing negative bias, and CZ broadening is shifting energy into the shadow zones, which is a positive bias. The shallow source has more transmission loss to attenuation in the seafloor, and the negative bias values associated with that TL keep the shallow-source Φ_b near zero, despite the positive influence of CZ broadening. For the deeper source, the bottom loss is not as significant, so the CZ broadening is the dominant process influencing the deep-source Φ_b.

From Figures 28-31 and Table 5, the Φ_{RMS} values for the 50m source are about two decibels for the low frequency case and about between five and six decibels for the high frequency case. The deeper source depth has Φ_{RMS} values greater than three decibels for the low frequency case and near six decibels for the higher frequency case. Despite the frequency dependence, the deeper source depth consistently experienced

41

higher variability than the shallower source depth. The differences in Φ_{RMS} are significant because the expected uncertainty is approximately 8%, or less than one decibel.

To sum up this section, factors that increase both Φ_b and Φ_{RMS} are higher frequency and deeper source depth. The spectrum used for the simulations does not appear to have a significant effect on acoustic variability.

C. OUT-OF-PLANE SCATTERING

There was not sufficient time in this study to simulate the range-dependent horizontal deflections that occur as sound transmits through eddies; however, the effect on beam-forming and target angle localization is significant, so some theory is discussed here. Much of this section is modified from Flatté and Colosi [2008], but it is thoroughly discussed in other literature as well [Munk 1980, Weinberg and Clark 1980, and Munk et al. 1995].

Using a ray-based physical model to simulate acoustic transmission, sound speed is represented as

$$c(x, y, z) = \bar{c}(z) + \delta c(x, y, z), \qquad (24)$$

where δc is a small perturbation when compared to $\bar{c}(z)$, the mean sound speed. The fractional sound speed change is defined as

$$\mu = \frac{\delta c}{c_0}. \qquad (25)$$

Horizontal angular deviations of rays due to refraction through sound speed fluctuations can be derived from the ray equations:

$$\frac{d\theta}{dx} \simeq -\frac{\partial \mu}{\partial y} = -\mu', \qquad (26)$$

where $-\mu'$ scales as $\dfrac{\mu}{L_y}$ and is the random gradient of fractional sound speed (in the y-direction). The deviation after traveling a distance dx is approximately $d\theta \simeq -\mu' dx$.

In order to convert this angular deviation into horizontal out-of-plane distance, the integration must first be calculated in time, where the angle of the ray at range R is:

$$\theta(R) \simeq -\int_0^R \mu'(x)dx. \tag{27}$$

Here, the integration in time over the perturbed ray path $s(t)$ is approximated as the integration over range of the unperturbed ray path. This approximation leads to a useful form of variance in ray angle:

$$\begin{aligned}\langle\theta_h^2\rangle &= \int_0^R dx_1\int_0^R \langle\mu'(x_1)\mu'(x_2)\rangle dx_2 \\ &\simeq \int_0^R \langle\mu^2\rangle\frac{L_H}{L_y^2}dx = \langle\mu^2\rangle\frac{L_H R}{L_y^2} = \langle\mu^2\rangle\frac{R}{L_y}.\end{aligned} \tag{28}$$

This form of the integration uses L_H and L_y to represent the correlation lengths along the ray, $L_H = L_y$, and assumes that the correlation length of the sound speed gradient is negligible compared to range, R. As shown above, the RMS angle variance in the horizontal grows as the square-root of range. Taking typical eddy-scale values, $\langle\mu^2\rangle = 2\times10^{-5}$ and $L_y = 50$ km, the RMS horizontal angle is approximately equal to:

$$\langle\theta_h^2\rangle^{1/2} \sim 0.8° \text{ (R/500 km)}^{1/2} \tag{29}$$

at a range of 500km.

When compared to an internal wave horizontal angle deviation representative of similar ocean conditions ($\langle\mu2\rangle$=4.0x10^{-7} and $L_H = 10$ km),

$$\langle\theta_h^2\rangle^{1/2} \sim 0.25° \text{ (R/500 km)}^{1/2}, \tag{30}$$

the angular deviation caused by eddies is significantly greater, nearly by a factor of three.

Using the small angle approximation to calculate range error from angular deviation, δy is approximately equal to $R\delta\theta$, as shown in Figure 32, where $\delta\theta = \langle\theta_h^2\rangle^{1/2} = \langle\mu^2\rangle^{1/2}\left(\dfrac{R}{L_y}\right)^{1/2}$. Combining the formulas above,

$$\delta y = \left(\frac{\langle\mu^2\rangle}{L_H}\right)^{1/2}\left(\frac{R}{500 \text{ km}}\right)^{3/2}, \tag{31}$$

and using typical eddy-scale values, the RMS range error at 500 km due to ocean eddies is

$$\delta y = 7 \text{ km} \left(\frac{R}{500 \text{ km}} \right)^{3/2}. \tag{32}$$

When compared to an internal wave range error representative of similar ocean conditions as above,

$$\delta y = 2.3 \text{ km} \left(\frac{R}{500 \text{ km}} \right)^{3/2}, \tag{33}$$

the range error at 500 km caused by eddies is significantly greater, by a factor of three.

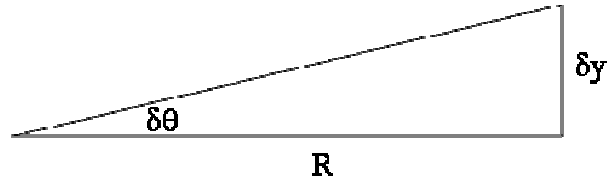Figure 32.   Angular deviation, $\delta\theta$, where R is unperturbed range and δy is range error due to angular deviation.

The scientific community has put much effort into quantifying internal wave effects on acoustic transmission. The above demonstration shows that ocean mesoscale features, such as eddies, are at least as important as internal waves in causing horizontal variations in acoustic transmission.

44

V.   CONCLUSION

A.   CURRENT EXPERIMENT

A two-dimensional parabolic equation model was built to simulate acoustic transmission through mesoscale environments in the Philippine Sea. The model used three essential parts. The background ocean was based on climatological ocean profiles for the Philippine Sea. The eddy fields were constructed using two wavenumber spectra: Stammer spectrum with correlation length 150km and Lorentzian spectrum with correlation length 50km. These eddy fields were then overlaid on the background ocean. Next, the acoustic portion of the model was incorporated using parabolic-equation propagation of a Gaussian sound source. Global altimetry data revealed that approximately 15cm of RMS variability in sea surface elevation exists in the Philippine Sea. This sea surface variability represents local oceanic kinetic energy. Based on Wunsch's vertical partitioning of oceanic energy, 20% of kinetic energy was modeled in the barotropic modes and 80% in the baroclinic modes. The baroclinic energy was then further partitioned into the first four baroclinic modes. Eddies were simulated as a linear superposition of Rossby waves of the first four baroclinic modes. This model was used to analyze acoustic propagation fluctuations through the background (climatological) ocean and the perturbed (eddy-field) ocean.

Eight different combinations of acoustic frequency (20Hz and 250Hz), eddy wavenumber spectra (Stammer or Lorentzian), and source depth (50m or 200m) were simulated through this model. For each combination, the model was run for 32 random realizations of eddy fields. For each of these realizations, a point-to-point transmission loss (TL) curve was calculated from source depth (50m or 200m) to a receiver at 50m. This TL curve was also calculated for the unperturbed ocean. These curves were smoothed in range using a Butterworth filter to eliminate the variability associated with multipath interference. From the 32 perturbed curves, a composite eddy-field TL curve was derived, and then this curve was differenced from the unperturbed curve to assess the acoustic variability caused by the mesoscale ocean features.

Several physical phenomena influence the patterns of transmission loss that are examined in this study. Evanescent waves occur outside of the convergence zones, and they decay much less with low frequency signals. This causes the cluttered appearance of the low frequency full water-column TL plots. Low frequency signals also experience more diffraction than higher frequency transmissions, leading to broader convergence zones. Conversely, high frequency signals experience stronger focusing near the surface, so these simulations show much stronger CZ rings near the surface. The high frequency signals have a smaller-scale interference pattern due to their shorter wavelengths. This creates the appearance of several lobes of energy within the main CZ beam in the TL plots.

Four physical mechanisms caused by eddies influence TL. Φ_b is a measure of the convergence zone broadening, driving energy into the seafloor, and trapping energy in the surface duct. Φ_{RMS} measures the fourth mechanism – scintillation.

The computer simulations revealed higher frequency sound transmitting through the eddy fields and deeper source depths cause the largest amount of acoustic variability, both in the bias (Φ_b) and in the RMS variability (Φ_{RMS}). These results suggest that acoustic variability through eddies is strongly dependent on frequency and weakly dependent on source depth. Somewhat surprisingly, the wavenumber spectrum used to simulate eddies had no significant effect on the acoustic variability beyond that which was already caused by the frequency or source depth.

The frequency dependence is so strong because the convergence zone shifting is highly frequency dependent. Low frequencies already have broad CZs due to diffraction, so the eddy fields do not have as much an impact, while for the higher frequency signals, the CZ are significantly broadened due to the eddies. In addition, the lower frequency signal was less likely to get trapped in the surface duct, which was another factor that limited its Φ_b. The higher frequency is more likely to split into micro-rays, which increases its Φ_{RMS}.

The spectrum dependence is insignificant, but revealed an area for further study. Clearly, travel time and intensity are more sensitive to different spectra of ocean features, so more clarity is required before any modeling decisions are based on eddy wavenumber spectra.

Source depth weakly impacts the trends for Φ_b and Φ_{RMS}. The CZ spreading causes a positive bias, while energy trapped into the seafloor causes a negative bias. Increased scintillation and surface duct trapping do not appear to influence Φ_b or Φ_{RMS} trends as they relate to source depth.

The simulations for this study revealed fluctuations of sound intensity of 5-20dB, which are significant to naval applications for the impact to detection methods and capabilities. For the upcoming NPAL field experiment in the Philippine Sea, the significance applies more to the usefulness of the tomographic data collected and how to best process that data at the conclusion of the experiment's field work. It also validates the plan to map the mesoscale features of the Philippine Sea, because a significant advantage can be gained through accurate knowledge of the mesoscale.

A final area of consideration is the horizontal out-of-plane refraction caused by eddies. This can cause a horizontal shift on order one degree at 500km, which is about 7km of localization error at 500km.

B.   FUTURE RESEARCH

Eddy effects on horizontal out-of-plane scattering are important because they affect beam-forming and target localization accuracy. Additional computer simulation of these effects is necessary to improving acoustic operations in a mesoscale-rich environment.

Some questions that this study uncovered also warrant further research. Despite the large difference in sea surface elevation correlation lengths (and corresponding eddy size) caused by the two different spectra (Stammer and Lorentz), there was little discernable difference in the acoustic variability caused by each spectrum. Further investigation into the variables that impact acoustic variability should be pursued.

47

The model developed here should be compared to existing acoustic models to determine the impact of the mesoscale environment beyond what is already being modeled. Additionally, these computer simulations need to be compared to actual acoustic data to see if nature reinforces the principles suggested by the simulations. However, the comparison becomes difficult because it is nearly impossible to separate eddy effects from other mesoscale effects such as internal waves in real ocean data.

A fourth area of research is in practical application of these findings. Tactically, how does the crew of a submarine exploit the ocean variability to make their own ship less detectable while simultaneously expanding their ability to detect enemy vessels?

A useful outcome of the NPAL experiment will be actual measurements of the proportional mode energy and baroclinic structures of eddies, as well as the important scales of eddies for acoustics. This is important to compare to the theory presented by Cornuelle and Howe [1987] that waves with lengths comparable to the ray loop length are most acoustically significant.

The horizontal out-of-plane scattering has important impacts on beam-forming capabilities. The horizontal coherence length is dictated by $\langle \theta^2 \rangle$ and the local wavenumber:

$$y_0{}^2 = \frac{\langle \theta^2 \rangle}{k_0{}^2} \tag{34}$$

where $\langle \theta^2 \rangle$ is the RMS angle deviation (described in Chapter IV, Section C) and k_0 is the local wavenumber. Based on the angle deviation presented here, what are the effects to beam-forming coherence?

Preliminary results presented here demonstrate that ocean eddies, especially the powerful ones in the Philippine Sea, can cause significant fluctuations to acoustic transmission loss in the ocean. With further research, acoustic prediction models can evolve from range-independent to high-resolution, eddy-resolving, range-dependent models, which will be important in truly understanding the ocean battlespace and exploiting that knowledge to naval tactical advantage.

LIST OF REFERENCES

Colosi, J. A. and S. M. Flatté, 1996: Mode Coupling by Internal Waves for Multimegameter Acoustic Propagation in the Ocean. *J. Acoust. Soc. Am.*, **100**, 3607-3620.

Commander, Navy Warfare Development Authority, 2006: *Navy Supplement to the DoD Dictionary of Military and Associated Terms*, Department of the Navy, Office of the Chief of Naval Operations, Washington DC, 244.

Cornuelle, B. and B. M. Howe, 1987: High Spatial Resolution in Vertical Slice Ocean Acoustic Tomography. *J. Geophys. Res.* **92**, 11680-11692.

Flatté, S. M., 1979: *Sound Transmission through a Fluctuating Ocean*, Cambridge University Press, Cambridge, 299.

Flatté, S. M. and J. A. Colosi, submitted 2008: Anisotropy of the Wavefront Distortion for Acoustic Pulse Propagation through Ocean Sound-Speed Fluctuations: A Ray Perspective.

Harrison, C. H. and J. A. Harrison, 1995: A Simple Relationship between Frequency and Range Averages for Broadband Sonar. *J. Acoust. Soc. Am.*, **97**, 1314-1317.

Jensen, F. B., W. A. Kuperman, M. B. Porter, and H. Schmidt, 2000: *Computational Ocean Acoustics*, Springer-Verlag, Inc., New York, 578.

Kirby, G. J., 1988: Some Range Dependent Effects in Sonar Performance. *Acous. Bul.*, 12-15.

Kobashi, F. and H. Kawamura, 2001: Variation of Sea Surface Height at Periods of 65-220 Days in the Subtropical Gyre of the North Pacific. *J. Geophys. Res.* **106**, 26817-26831.

Munk, W, P. Worcester, and C. Wunsch, 1995: *Ocean Acoustic Tomography*. Cambridge University Press, Cambridge, 433.

Munk, W. H., 1980: Horizontal Deflection of Acoustic Paths by Mesoscale Eddies. *J. Phys. Oceanogr.*, **10**, 596–604.

Qui, B., 1999: Seasonal Eddy Field Modulation of the North Pacific Subtropical Countercurrent: TOPEX/Poseidon Observations and Theory. *J. Phys. Oceanogr.* **29**, 2471-2486.

Smith, K. B., M. G. Brown, and F. D. Tappert, 1992: Acoustic Ray Chaos Induced by Mesoscale Ocean Structure. *J. Acoust. Soc. Am.*, **91**, 1950-1959.

Stammer, D., 1997: Global Characteristics of Ocean Variability Estimated from Regional TOPEX/POSEIDON Altimeter Measurements. *J. Phys. Oceanogr.*, **27**, 1743-1769.

Vastano, A. C. and G. E. Owens, 1973: On the Acoustic Characteristics of a Gulf Stream Cyclonic Ring. *J. Phys. Oceanogr.*, **3**, 470-478.

Weinberg, N. L. and J. G. Clark, 1980: Horizontal Acoustic Refraction through Ocean Mesoscale Eddies and Fronts. *J. Acoust. Soc. Am.*, **68**, 703-705.

Worcester, P. F. and R. C. Spindel, 2005: North Pacific Acoustic Laboratory. *J. Acoust. Soc. Am.*, **117**, 1499-1510.

Wunsch, C., 1997: The Vertical Partition of Oceanic Horizontal Kinetic Energy. *J. Phys. Oceanogr.*, **27**, 1770-1794.

INITIAL DISTRIBUTION LIST

1.   Defense Technical Information Center
        Ft. Belvoir, Virginia

2.   Dudley Knox Library
        Naval Postgraduate School
        Monterey, California

3.   Professor John A. Colosi
        Naval Postgraduate School
        Monterey, California

4.   Professor Jeffrey D. Paduan
        Naval Postgraduate School
        Monterey, California

5.   Professor Mary Batteen
        Naval Postgraduate School
        Monterey, California

6.   Professor Peter Worcester
        University of California at San Diego
        San Diego, California

7.   Professor James Mercer
        University of Washington
        Seattle, Washington

8.   Professor Arthur Baggeroer
        Massachusetts Institute of Technology
        Cambridge, Massachusetts